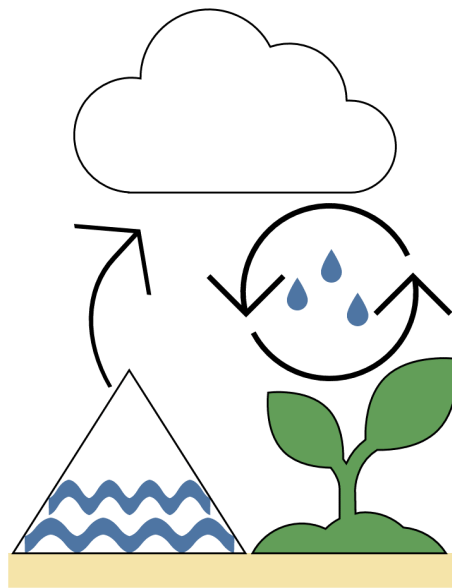


Making it Rain in the Desert: Fantasy or Future?

The Potential of Restoring the Water Cycle in Arid Regions
by Enhanced Evaporation through Technology



Sarah Warnau

Daily supervisor: MSc. Jolanda Theeuwen, Wetsus
Project supervisor: Dr. Aarnout van Delden, Utrecht University
Second supervisor: Dr. Michiel Baatsen, Utrecht University
Additional advisor: Prof. dr. ir. Bert Hamelers, Wetsus

A Climate Physics Master's thesis

Institute for Marine and Atmospheric Research Utrecht
Utrecht University
July, 2022



Making it Rain in the Desert: Fantasy or Future?

The Potential of Restoring the Water Cycle in Arid Regions by
Enhanced Evaporation through Technology

Sarah Warnau

Abstract

Regreening initiatives are being undertaken as climate change mitigation strategies, to improve water and food security, and to increase biodiversity. Because of positive feedback loops between vegetation and precipitation, regreening has the potential to lead to the restoration of local and regional water cycles. However, in arid and hyper-arid regions, the amount of available rainwater is not sufficient to sustain the initial stages of regreening. A technology that uses solar energy to evaporate seawater may be able to enhance convective rainfall. The main research question is: Can evaporation through technology potentially be used for water cycle restoration in arid and hyper-arid regions?

Using atmospheric boundary layer theories as described by Stull (1988), a simple atmospheric column model was developed and coupled to a surface model with a dynamic vegetation component. Results of sensitivity analyses with this numerical model show the importance of atmospheric conditions and it is found that evaporation through technology has the potential to be effective in regions with a relatively moist and cold atmosphere. Regions that satisfy these conditions and also have a dry soil are mostly found 25-35°N near coasts and/or in mountainous areas.

One such area is the Sinai Peninsula. Numerical simulations using ERA5 reanalysis data as boundary conditions show that the evaporation technology can increase precipitation locally, but this increase is small. However, because of the wind directed southward and up the mountain range of South Sinai, the technology has the potential to cause precipitation non-locally as well as is shown by simulations where the atmospheric column is moved along a streamline.

In conclusion, enhanced evaporation through technology has the potential to be used for regreening projects if atmospheric conditions are favorable. However, more research is needed and the potential adverse effects, such as warming, need to be taken into consideration.

Contents

1	Introduction	7
2	Theory	9
2.1	Feedbacks	9
2.2	Radiation balance at the surface	11
2.3	The atmospheric boundary layer	12
2.3.1	The convective boundary layer slab model	12
2.3.2	The residual layer and nocturnal boundary layer	14
2.4	Cloud formation and precipitation	15
2.5	Surface processes	16
3	Methods	20
3.1	Model	20
3.1.1	Surface model	20
3.1.2	Atmospheric column model	20
3.1.3	Boundary processes	22
3.1.4	<i>Open, closed, and moving column</i> modes	23
3.2	Sensitivity analysis	24
3.3	Case studies	24
3.3.1	Case study selection	24
3.3.2	Data and parameter tuning	25
3.3.3	Model runs	25
4	Results	27
4.1	Sensitivity analysis	27
4.1.1	Introduction	27
4.1.2	Closed model modes	27
4.1.3	Open model mode	30
4.1.4	Summary	30
4.2	The technology	33
4.2.1	Introduction	33
4.2.2	Sensitivity to the technology's variables	33
4.2.3	Summary	35
4.3	Where technology can be effective	38
4.3.1	Introduction	38
4.3.2	Sensitivity analysis in OMTL and OMTM modes	38
4.3.3	Where can the technology be effective?	42
4.3.4	Summary	42

4.4	Case study: Sinai peninsula	45
4.4.1	Introduction	45
4.4.2	Parameter tuning	45
4.4.3	Open model mode	46
4.4.4	Moving column mode	46
4.4.5	Comparison with reanalysis data	47
4.4.6	Summary	48
5	Discussion	51
5.1	Introduction	51
5.2	The results	51
5.3	The model	52
5.4	The data	53
5.5	The technology	54
5.6	General outlook	54
6	Conclusion	56
	Acknowledgements	57
	Bibliography	58
A	Table of used symbols	61
B	Methods	64
B.1	Additional formulas	64
B.1.1	Solar radiation	64
B.1.2	Temperature, pressure, and density	64
B.2	Overview of data used	65
C	Results	66
C.1	CM sensitivity	66
C.2	OM sensitivity	68
C.3	OMT sensitivity	71
C.4	Case studies	72
C.5	Discussion	80

Acronyms

ABL	Atmospheric boundary layer, see Chapter 1
CBL	Convective boundary layer, see Section 2.3.1
CM1	Closed model, variant 1, see Section 3.1.4
CM2	Closed model, variant 2, see Section 3.1.4
MCM	Moving column mode, see Section 3.1.4
NBL	Nocturnal boundary layer, see Section 2.3.2
OM	Open model, see Section 3.1.4
OMT	Open model with technology, see Section 3.1.4
OMTH	Open model with high evaporating technology, see Section 3.1.4
OMTL	Open model with low evaporating technology, see Section 3.1.4

1 | Introduction

The current decade has been declared the *United Nations Decade on Ecosystem Restoration* with the aim of preventing, halting and reversing the degradation of ecosystems worldwide [23]. In this context, a wide variety of activities is undertaken, including the restoration of ecological processes and the combat of desertification [23]. Examples of such initiatives are *Justdigg* [17] and *the Great Green Wall* [36] that both aim to regreen desert regions and increase water and food security, biodiversity, and resilience of local communities to climate change.

The main theory behind regreening initiatives is that it stimulates a positive feedback loop between water retention, vegetation, evapotranspiration, and rainfall [38]. Land degradation and desertification lead to little vegetation and little water in the system. By increasing the water retention and planting vegetation, the water cycle can be restored. This theory is supported by observational studies in e.g. the Beichuan River Basin in China [39].

Initiatives as *Justdigg* and *the Great Green Wall* often make use of natural regreening techniques that depend on the availability of rainwater. This dependence limits such regreening activities to semi-arid regions where the amount of water available through precipitation is enough to sustain a water level in the soil above the wilting point: the minimum amount of water needed to have plant growth [32].

Arid or hyper-arid regions have a 5 times higher climatic demand for water than they receive through precipitation [7]. For regreening attempts in these regions, an external source of freshwater is needed. Using desalination of seawater for direct irrigation is an energy intensive and therefore costly method [2]. A different approach would be to increase the atmospheric water vapor content with the goal of stimulating cloud formation and precipitation. To this end, a technology is being developed that produces water vapor from brackish or seawater, via direct evaporation, driven by solar energy [1].

However, increasing the amount of atmospheric water vapor does not directly lead to the formation of clouds and precipitation. Therefore, it is uncertain if enhanced evaporation through technology can be used for regreening projects in arid and hyper-arid regions. In this Master's project I will seek to answer the following research question: **Can evaporation through technology potentially be used for water cycle restoration in arid and hyper-arid regions?** I will be using a simple atmospheric boundary layer (ABL) model with parameterizations for cloud formation and precipitation, coupled to a surface model.

The research is structured around four sub questions:

1. What is the sensitivity of the model to different parameters, initial conditions, and boundary conditions?

2. Under which conditions can enhanced evaporation through technology be effective?
3. Which hyper-arid or arid regions fit the conditions resulting from subquestion 2?
4. Does enhanced evaporation through technology have the potential to be used for water cycle restoration in the identified regions?

Using a sensitivity analysis, I will answer the first two sub questions and identify the variables that determine the effectiveness of the enhanced evaporation through technology: does it enhance rainfall, does it create favorable conditions for plant growth, and can the water cycle be restored? With those results, I will identify regions where this technology could be effective, answering the third subquestion. Using the model and data from one of the identified regions, the effectiveness of the enhanced evaporation in this region can be determined, answering the last sub question.

Several modelling experiments have been conducted to find the variables that affect the transition between the dry and moist states of a system. According to an experiment with a coupled surface-ABL model by Konings, Katul, and Porporato [21], the transition between a completely dry state and a wet-tropical state is a function of free atmosphere parameters, and is more sensitive to the atmospheric humidity profile than the temperature profile. Because of the similarity between the model used by Konings, Katul, and Porporato [21] and the model that is going to be used in this thesis project, it can be expected that the same results will be found.

Seneviratne et al. [32] found that studies on soil moisture-precipitation coupling since the 1990s have emphasised the role of indirect interactions, rather than moisture recycling. One example is that additional precipitated water falling over wet soils may be triggered by water vapor from surface fluxes, but originates from oceanic sources [32]. An experiment with a coupled surface-ABL model by Bonetti et al. [4] showed that if the source of water vapor within the ABL originates from surface fluxes, then lowering the water content of the soil will suppress rainfall. On the other hand, when the source of water vapor in the ABL is supplied by the free atmosphere, then lowering the water content of the soil will lead to increased rainfall due to an increase in ABL height. These findings suggest that enhanced evaporation through technology could either be effective or repressive in regions with a relatively moist free atmosphere. This depends on the strength of the regional moisture recycling.

“Hotspots” of regionally strong precipitation feedbacks are observed in transitional zones (grasslands and savannas), such as semi-arid and monsoonal regions, and in regions where orographic lift drives precipitation events [38]. Therefore, the expectation is that when the free atmosphere contains enough humidity, e.g. certain arid regions, and the regional moisture recycling is sufficiently high, that enhanced evaporation through technology can potentially be used for water cycle restoration. In hyper-arid regions, the free atmosphere will probably often contain very little moisture, and thus the expectation is that it is only possible to generate precipitation and potentially restore the water cycle here when orography and wind are favorable.

2 | Theory

2.1 Feedbacks

There are several hydrological feedbacks between the atmosphere and the surface, two of which are shown in Figure 2.1A. In the soil, vegetation cover enhances the infiltration capacity due to changes in the soil (e.g. because of the roots) [38]. Enhanced infiltration has a positive effect on the soil moisture availability for plants and therefore increases the vegetation productivity [38]. This is called the micro-scale feedback. On the macro-scale, increased amounts of water in the soil and an increase in vegetation both increase the amount of water vapor in the atmosphere through evaporation and transpiration which could lead to increased precipitation [38]. These feedbacks cause the relation between vegetation and precipitation to be nonlinear (Figure 2.1B) and sometimes discontinuous (Figure 2.1C) [38]. In this research, only the macro-scale feedback will be further considered.

The macro-scale feedback can be divided into two separate pathways: the radiative and the evapotranspiration feedback. These feedbacks lead from increased biomass to increased precipitation [20]. The radiative feedback states that an increase in vegetation has a negative effect on the albedo of the surface and therefore decreases the amount of shortwave radiation from the sun that is reflected back to the atmosphere. This extra energy at the surface is released in the form of turbulent fluxes that cause an increase of convection and humidity and thereby increase the chance of precipitation. The evapotranspiration feedback states that an increase in vegetation directly increases the latent heat flux, which increases the humidity of the atmosphere [20].

However, Seneviratne et al. [32] note that these soil moisture-precipitation feedbacks are not always positive, but can potentially be negative because increasing evapotranspiration decreases the available soil moisture. In order to sustain a positive feedback, it is not sufficient that enhanced soil moisture and evapotranspiration lead to additional precipitation, because the enhancement in precipitation needs to be at least equivalent to the enhancement in evapotranspiration or else the net effect will be a reduction of the original soil moisture anomaly [32]. A measure for this relationship is the precipitation to evaporation ratio

$$\psi = \frac{\text{precipitation}}{\text{evaporation}} \quad (2.1)$$

ψ is measure of strength of hydrological land surface-atmosphere coupling and can be used to identify local, regional, or distant rainfall responses to surface evaporation and transpiration [38].

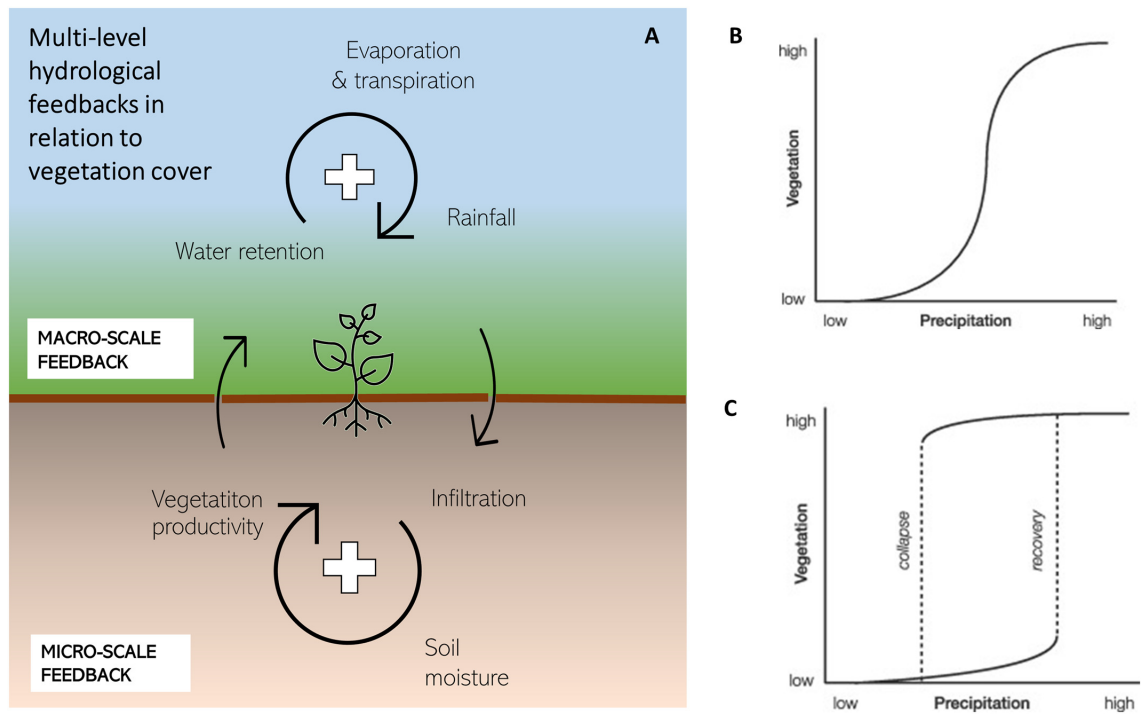


Figure 2.1: From Wierik et al. [38]. Two hydrological feedbacks related to vegetation. Panel A shows the micro scale positive feedback between vegetation cover, which increases infiltration through changing the soil, which in turn increases the amount of soil moisture and finally the vegetation productivity. Also, a macro-scale feedback exists between the increased water retention due to vegetation, which leads to an increase in evaporation and transpiration, which in turn can increase the amount of rainfall. These feedbacks depend on and are linked through vegetation. Panels B and C shows the relation between precipitation and vegetation which is non-linear and can be discontinuous as shown in panel C.

2.2 Radiation balance at the surface

The surface energy balance can be written as the sum of shortwave radiative fluxes R_{SW} , longwave radiative fluxes R_{LW} , turbulent fluxes of sensible heat SHF and latent heat LHF , and the subsurface heat flux G (all in W m^{-2}):

$$\underbrace{R_{SW,in} - R_{SW,out} + R_{LW,in} - R_{LW,out}}_{R_n} - SHF - LHF - G = 0 \quad (2.2)$$

where the first four terms combined are the net radiation R_n .

Assuming the surface emits as a perfect black body, the net radiation $R_n(t)$ at a certain time t is given by

$$R_n(t) = (1 - \alpha)R_s(t) + \varepsilon_s(\varepsilon_a\sigma T_{air}^4 - \sigma T_s^4) \quad (2.3)$$

where α is the surface albedo, $R_s(t) = R_{SW,in}(t)$ is the incoming shortwave radiation, $\varepsilon_s = 1$ is the surface emissivity, ε_a the atmospheric emissivity, σ the Stefan-Boltzmann constant, and T_s the surface temperature [20]. The first term in equation 2.3 represents the available shortwave radiation and the second term the available longwave radiation at the surface.

Because it is difficult to specify ε_a and T_{air} for a whole column, T_{air} is chosen at 2 m, and the following parameterization is used for ε_a

$$\varepsilon_a = 0.552e^{(1/7)} \quad (2.4)$$

where e is the water vapor pressure at 2 m in hPa [15, 6]. The effect of cloud cover on radiation is neglected.

The incoming shortwave radiation is calculated using longitude and latitude and the time of the year following Heerwaarden [11] and can be found in appendix B.

The surface sensible heat flux depends on the gradient between surface and air temperatures [20]:

$$SHF = \frac{\rho_{air}c_p}{r_a}(T_s - T_{air}) \quad (2.5)$$

where r_a is the atmospheric resistance and T_{air} is the air temperature. From this equation the evolution of the surface temperature can be calculated. Note that $T_{air} \approx \theta$ near the surface by definition.

SHF can be determined as the residual of the surface energy balance

$$SHF = R_n - LHF - G \quad (2.6)$$

where G is the subsurface or ground heat flux [20]. The ground heat flux can be an important heat sink during the day and an important heat source at night. The daily cycle is not synchronous with the forcing, but this is often neglected and it is assumed that the G is a fraction of R_n [21, 20, 35].

Vegetation coverage changes the albedo of the surface. Desert areas without vegetation have a higher albedo than vegetated areas. A simple way to model this is by linearly interpolating the albedo between α_{max} at $B = 0$, and α_{min} at $B = B_{max}$, where B is the amount of biomass in kg/m^2 and the *min* and *max* subscripts indicate the minimum and maximum possible values for a certain region [20].

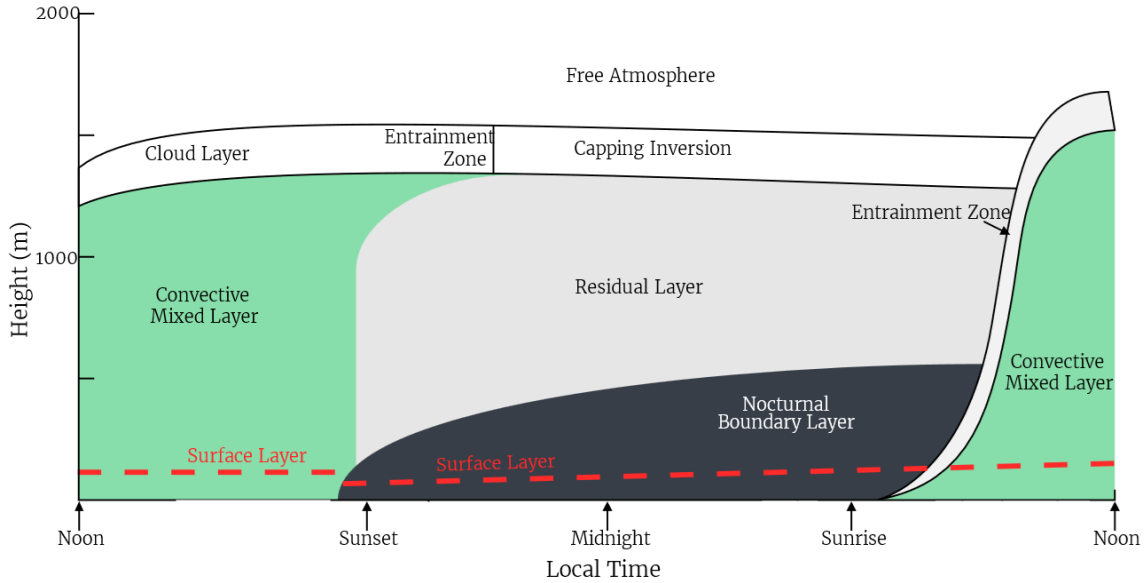


Figure 2.2: Stull [35] distinguishes three major parts of the atmospheric boundary layer over land: “a very turbulent mixed layer; a less-turbulent residual layer containing former mixed-layer air; and a nocturnal stable boundary layer of sporadic turbulence. The mixed layer can be subdivided into a cloud layer and a subcloud layer.” Figure adapted from Stull [35] by NikNaks. License: CC BY-SA 3.0

2.3 The atmospheric boundary layer

The atmospheric boundary layer (ABL, Figure 2.2) is the part of the troposphere that is directly influenced by the earth’s surface, and responds to surface forcings with a timescale of about an hour or less [35]. This leads to a pronounced daily cycle in nearly all meteorological variables such as wind, temperature, moisture and other scalars such as chemical compounds [24]. This is in contrast to the free atmosphere that is above the ABL, which does not show these cycles. The ABL is capped with an inversion layer. During the day entrainment takes place through this layer and it is then called the entrainment layer [35].

The ABL roughly makes up the lowest 10% of the troposphere and varies in depth between several hundreds of meters to several kilometers. Over desert regions during the day, boundary layers are usually higher: Little evaporation and a very hot surface lead to strong convection which results in a higher ABL. During the night, convective turbulence decreases to the point where turbulence can not be maintained against dissipation, and eventually decays completely [35]. The convective layer is then reclassified as the residual layer [35].

2.3.1 The convective boundary layer slab model

A slab model is a simple approximation of the convective boundary layer (CBL), where it is assumed that CBL is well mixed regarding potential temperature (θ) and specific humidity (q), and has height h (Figure 2.3). The inversion or entrainment layer at the top of the CBL is assumed to be of negligible depth.

Above the inversion layer is the free atmosphere. An often made approximation of the free atmosphere is that θ and q change linearly with height above the surface

(z) such that

$$\theta(z) = \gamma_\theta z + \phi_\theta \quad (2.7)$$

$$q(z) = \gamma_q z + \phi_q \quad (2.8)$$

where γ and ϕ are the sets of slopes and intercepts respectively [20, 27].

To first order, air density in the CBL can be assumed constant, which allows for the use of volume conservation in place of mass conservation [35]. Inflow can occur in the vertical because of entrainment at the top of the CBL and in the horizontal because of convergence within the CBL [35]. Convergence can be written in terms of the mean large scale vertical motion (w_L) acting at the top of the CBL. When active clouds are present that vent air out of the top of the CBL, the volume conservation equation becomes

$$\frac{dh}{dt} = (1 - \sigma_A)w_e - \sigma_A w_c + w_L \quad (2.9)$$

where σ_A is the fraction of the sky covered by active clouds, w_c is the average vertical velocity within the clouds at the CBL top, and w_e is the entrainment velocity, which is the average vertical velocity at the top of the CBL. Without clouds and subsidence, the CBL top rises at a rate equal to the entrainment velocity [35].

The conservation of potential temperature and humidity in the CBL leads to the following simple conservation equations in integrated form:

$$h \frac{d\langle\theta\rangle}{dt} = \overline{(\theta'\omega')_s} - \overline{(\theta'\omega')_h} \quad (2.10)$$

where $\overline{(\theta'\omega')_s} = SHF/\rho_{air}c_p$ with SHF the sensible heat flux, ρ_{air} the density of air, and c_p the specific heat of air [20, 25, 35]. The angle brackets $\langle \rangle$ denote the average value of a quantity over the depth of the mixed CBL. For the water balance in the CBL we get:

$$h \frac{d\langle q \rangle}{dt} = \overline{(q'\omega')_s} - \overline{(q'\omega')_h} \quad (2.11)$$

where $\overline{(q'\omega')_s} = LHF/\rho_{air}\lambda$ is the surface latent heat mass flux where LHF is the latent heat flux and λ the latent heat of vaporization of water [20, 25, 35].

The fluxes at the surface can be found using the surface model (Sections 2.2 and 2.5). The fluxes at the top are the entrainment fluxes and are determined by the difference between the heat and humidity in the free atmosphere at $z = h$, and the heat and humidity of the CBL [20]. This gives us:

$$\overline{(\theta'\omega')_h} = -w_e(\theta_h - \langle\theta\rangle) \quad (2.12)$$

$$\overline{(q'\omega')_h} = -w_e(q_h - \langle q \rangle) \quad (2.13)$$

θ_h and q_h are the potential temperature and specific humidity values of the free atmosphere at the CBL top (Figure 2.3).

A prognostic equation for h can be found using only thermodynamics [35]:

$$\frac{dh}{dt} = \frac{1}{\gamma_\theta} \frac{d\langle\theta\rangle}{dt} = \frac{\overline{(\theta'\omega')_s} - \overline{(\theta'\omega')_h}}{\gamma_\theta h} \quad (2.14)$$

where γ_θ is the local value of $d\theta/dt$ just above the top of the CBL. With this equation, roughly 80-90% of the observed variation of the CBL height can be explained [35].

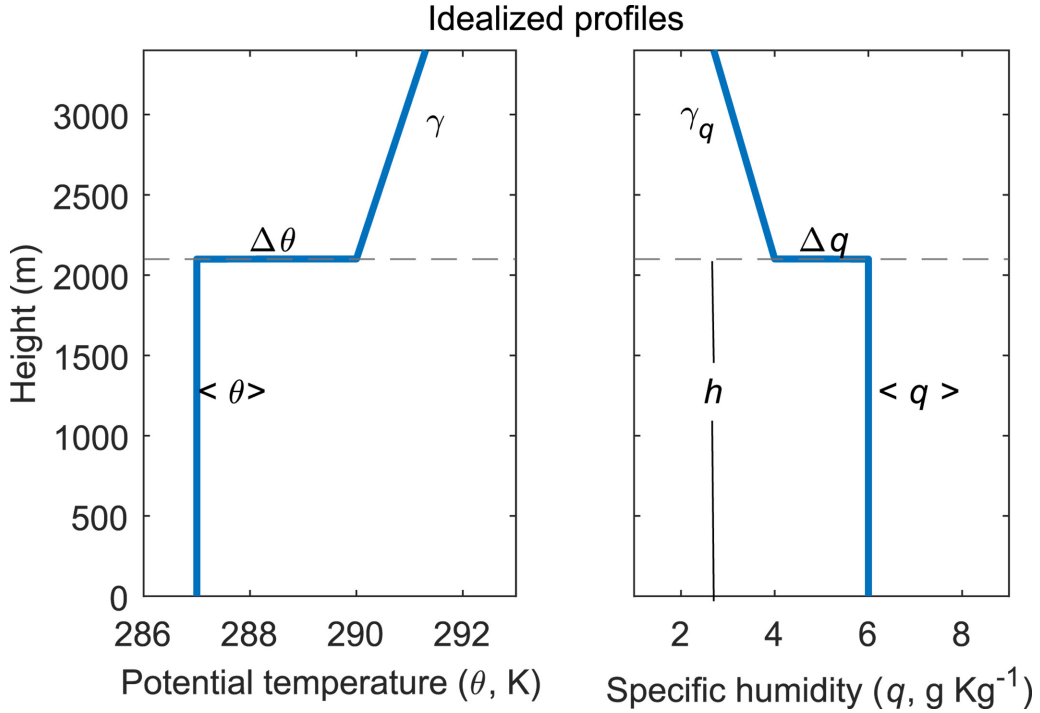


Figure 2.3: From Rey-Sanchez et al. [27]. Idealized potential temperature (θ) and specific humidity (q) profiles of convective boundary layer (CBL) slab models. $\Delta\theta = \theta_h - \langle\theta\rangle$ and $\Delta q = q_h - \langle q\rangle$ are the jumps in potential temperature and specific humidity at the entrainment zone. γ and γ_q are the lapse rates in the free atmosphere. $\langle \rangle$ denote average values across the CBL. The dotted line represents the height (h) of the CBL.

2.3.2 The residual layer and nocturnal boundary layer

In the evening, turbulence decays in the formerly well-mixed CBL. The resulting layer of air is called the residual layer because its initial mean state variables and concentration variables are the same as those of the recently decayed CBL [35]. The residual layer is neutrally stratified, resulting in turbulence that is nearly of equal intensity in all directions [35].

During the night, the nocturnal stable boundary layer (NBL) gradually increases in thickness by modifying the bottom of the residual layer. Often the NBL is not mixed but gets a more stable temperature profile during the night, as the surface cools. The evolution of the accumulated cooling ($\Delta\theta_s \cdot H_{\Delta\theta}$) is given by a heat balance of all forcings [35]:

$$-\frac{d\Delta\theta_s \cdot H_{\Delta\theta}}{dt} = Q_T \quad (2.15)$$

where Q_T is the total heat flux acting on the bulk NBL. The potential temperature profile can be described by a polynomial [35]:

$$\Delta\theta(z) = \left(1 - \frac{z}{h}\right)^n \Delta\theta_s \quad (2.16)$$

with $H_{\Delta\theta} = h/(n+1)$ and n determines the shape of the temperature profile in the NBL.

Where during the day the turbulent heat flux is the main heat source and radiative warming could be neglected, during the night this is not the case: Radiative cooling has to be considered. As a first approximation this cooling term (Q_R) can be expressed as

$$Q_R = a_1(\theta_s - \theta_m) \quad (2.17)$$

where a_1 is a proportionality constant, θ_m is the mean potential temperature of the NBL, and θ_s is the potential temperature of the surface [33].

The NBL evolution is hard to model because it does not have a clearly defined top [35]. A rate equation where the NBL grows towards an equilibrium height can be used [35]:

$$\frac{dh}{dt} = \frac{h_{eq} - h}{\tau} \quad (2.18)$$

where τ is a scaling time and has order of magnitude 7 to 30 hours [35].

2.4 Cloud formation and precipitation

The formation of precipitation in the atmosphere is a non-trivial physical process [29]. According to the Clausius-Clapeyron equation, air parcels containing water vapor will become saturated when their temperature decreases during ascent. The height up to which an air parcel has to be brought to become saturated is called the lifting condensation level. When a parcel ascends further than the lifting condensation level, water vapor will condensate and liquid water droplets will form. Condensation leads to latent heat release, which can give the parcel positive buoyancy.

When the top of the CBL crosses the lifting condensation level, condensation with rate k_1 will lead to the formation of liquid water (q_L) in the ABL and will cause the specific humidity to decrease. When there are cloud droplets but the air is unsaturated for water vapor ($q < q_{sat}$), the cloud droplets will evaporate with rate k_2 , increasing the specific humidity. These processes for the ABL column are captured in the following two equations:

$$C = k_1 \int_{z=0}^{z=h} q - q_{sat} dz \quad \begin{cases} k_1 > 0, & \text{for } q > q_{sat} \\ k_1 = 0, & \text{for } q \leq q_{sat} \end{cases} \quad (2.19)$$

$$E_c = k_2 \int_{z=0}^{z=h} q_L dz \quad \begin{cases} k_2 > 0, & \text{for } q < q_{sat} \\ k_2 = 0, & \text{for } q \geq q_{sat} \end{cases} \quad (2.20)$$

where C is the condensation rate and E_c is the evaporation rate of clouds. q_{sat} is the saturation specific humidity which can be found from the saturation mixing ratio with $q_{sat} = r_{sat}/(1 + r_{sat})$ [26]. r_{sat} is the saturation mixing ratio which is given by

$$r_{sat} = \frac{\epsilon e_{sat}}{p - e_{sat}} \quad (2.21)$$

where p is pressure and ϵ is the ratio between the specific gas constants for dry air and water vapor [8]. e_{sat} is the saturation vapor pressure and can be calculated using Tetens's formula, which is an empirical formula for realistically varying latent heat of vaporisation with temperature. It is given by [8]:

$$e_{sat} = 611.2 \exp \left\{ 17.67 \left(\frac{T_{air}[^\circ C]}{T_{air}[^\circ C] + 243.5} \right) \right\} \quad (2.22)$$

where T_{air} is the air temperature in °C. It can be found for every height from the potential temperature and pressure, which in turn can be found from the hydrostatic balance (Appendix B).

Once clouds develop, condensation nuclei are required to allow for rapid growth of water droplets [16]. When these water droplets reach sufficient size to precipitate and re-penetrate the unsaturated air below the cloud base without completely evaporating before reaching the ground surface, rainfall at the surface occurs [16]. Roughly, after h intersects the lifting condensation level, the entire process leading to precipitation detection at the ground may vary from minutes up to 2 hours [16].

Figure 2.4 shows an intuitive representation of clouds that are embedded within, and are an integral part of the CBL [35]. In this research, only this type of clouds are considered. The difference between the theoretical adiabatic value and the actual value in Figure 2.4d shows the effect of entrainment. Assuming there is no liquid water in the free atmosphere, we can define the dynamics of the liquid water content of the ABL as

$$\frac{d}{dt} \int_{z=0}^{z=h} q_L dz = C - E_c - w_e \cdot q_L(z=h) - k_3 \int_{z=0}^{z=h} \left(q_L - \frac{a_2}{\rho_{air}} \right) dz \begin{cases} k_3 > 0, & \text{for } q_L > \frac{a_2}{\rho_{air}} \\ k_3 = 0, & \text{for } q_L \leq \frac{a_2}{\rho_{air}} \end{cases} \quad (2.23)$$

where the last term represents the process of forming rain droplets from cloud droplets which is called autoconversion. This term comes from Kessler [18] who attempts to capture the microphysical processes governing the formation of rain by making a distinction between liquid water that forms clouds (q_L) and liquid water that forms rain (q_R). Note that q_L and q_R are not mixed in the CBL.

Kessler [18] models the formation of rain water through the simple reasoning that the rate of cloud autoconversion increases with the cloud density but is zero for amounts below some threshold. Such a process is defined by

$$\frac{d}{dt} \int_{z=0}^{z=h} q_R dz = -P + k_3 \int_{z=0}^{z=h} \left(q_L - \frac{a_2}{\rho_{air}} \right) dz \begin{cases} k_3 > 0, & \text{for } q_L > \frac{a_2}{\rho_{air}} \\ k_3 = 0, & \text{for } q_L \leq \frac{a_2}{\rho_{air}} \end{cases} \quad (2.24)$$

where P is the precipitation rate, k_3 is the cloud autoconversion coefficient, and a_2 is the cloud conversion threshold [18]. Various effects of nature can be represented by choices of k_3 and a_2 . In Kessler [18] $k_3 = 10^{-3} \text{ s}^{-1}$ and $a_2 = 0.5 \text{ g m}^{-3}$.

2.5 Surface processes

The calculation of moisture fluxes from the surface is complex as they depend on soil moisture, atmospheric moisture, land roughness, energy exchange, and indirectly on topography, soil properties and land use, all of which are highly heterogeneous and sometimes variable in time [29]. Since the latent heat flux from land is both a water and energy flux, soil moisture is both a water and energy storage [32]. The seasonal storage of subsurface water introduces long-term memory effects with timescales of several months [30]. This “soil moisture memory” is an important component in land–atmosphere interactions, and has thus been the topic of numerous observational and modelling investigations [32].

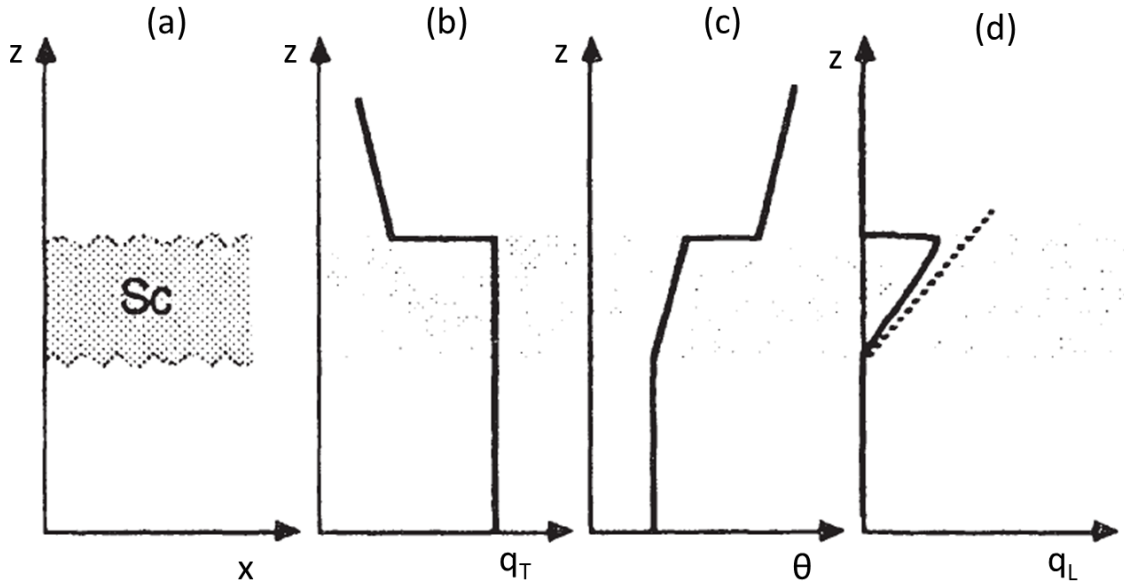


Figure 2.4: Adapted from Stull [35]: Idealized profiles of mean variables within a stratocumulus-topped mixed convective boundary layer. (a) cloud location; (b) total specific humidity (water vapor and liquid water); (c) potential temperature; (d) liquid water specific humidity (dashed line indicates the theoretical adiabatic value).

As discussed before (Section 2.1), vegetation plays an important role in the moisture feedbacks between atmosphere and surface. The dynamics of vegetation biomass (B) per unit area in a water (W) limited system can be modelled using

$$\frac{dB}{dt} = b B \eta(W) - d_1 B \quad (2.25)$$

where the first term on the right hand side is the growth term which has a soil moisture dependence in the form of the function $\eta(W)$. The last term is the death rate. It has been shown by Wang et al. [37] that this simple vegetation biomass model in combination with a soil water bucket model agrees with field measurements in a desert ecosystem in NW China. They used the following piecewise linear form for the soil moisture dependence:

$$\eta(W) = \begin{cases} 0, & \text{for } W < W_{wilt} \\ \frac{W - W_{wilt}}{W^* - W_{wilt}}, & \text{for } W_{wilt} < W < W^* \\ 1, & \text{for } W > W^* \end{cases} \quad (2.26)$$

where W_{wilt} is the wilting point and W^* is the point of incipient stomatal closure.

Subsurface water dynamics are determined by the influx of water through infiltration of rain water, and out fluxes of water drainage to the deep soil, transpiration by plants and soil evaporation. These processes are captured in the following equation

$$\frac{dW}{dt} = P - E_t - E_s - r_w W \quad (2.27)$$

where W is gained from precipitation and lost due to transpiration at rate E_t , soil evaporation at rate E_s , and deep soil drainage at rate $r_w W$, which is a simplification of the model used by Konings et al. [20]. Seneviratne et al. [32] note that there are exceptions to the simple relation between W and P : in cases of intense precipitation, when the precipitation rate is higher than the infiltration rate, precipitation anomalies result in runoff rather than soil moisture anomalies, which is not captured in the equation above.

The evaporation and transpiration rates can be calculated as

$$E_t = \frac{LHF_t}{\lambda \rho_{H_2O}} \quad (2.28)$$

$$E_s = \frac{LHF_s}{\lambda \rho_{H_2O}} \quad (2.29)$$

where λ is the latent heat of vaporization of water and ρ_{H_2O} is the density of water. LHF_t and LHF_s are the latent heat fluxes through transpiration and soil evaporation respectively.

The estimation of latent heat release is generally based on the Penman-Monteith equation [29, 22]. In canonical form it is

$$LHF = \frac{\Delta(R_n - G) + \frac{\rho_{air} c_p VPD}{r_a}}{\Delta + \gamma \left(1 + \frac{r_s}{r_a}\right)} \quad (2.30)$$

where ρ_{air} and c_p are the density and specific heat capacity of air, respectively, and $VPD = e_s - e$ is the vapor pressure deficit: the difference between the saturation vapor pressure e_s and the actual vapor pressure e [20, 22]. Δ is the slope of the Clausius-Clapeyron equation which relates the saturated vapor pressure of water to temperature [20]. $\gamma = c_p p_s / 0.622 \lambda$ is the psychrometric constant, where p_s is the surface pressure [20]. r_a is the aerodynamic resistance and r_s is the surface resistance, the inverse of the surface conductance g_s [20].

For the soil evaporation, the surface conductance is the conductance over bare soil g_s^{Es} , so $r_s = r_s^{Es} = 1/g_s^{Es}$ [20]. It is given by

$$g_s^{Es} = g_{max}^{Es} \frac{W}{W + W_{wilt}} \left(1 - \frac{B}{B + k_6}\right) \quad (2.31)$$

where g_{max}^{Es} is the maximum bare soil conductance and k_6 is the saturation constant for the evaporation reduction function due to shade from biomass, ignoring biomass morphology [20].

For transpiration, the surface conductance is the stomatal conductance g_s^{Et} , so $r_s = r_s^{Et} = 1/g_s^{Et}$ [20]. It captures the vegetation response to water stress. Using the method of Wang et al. [37] for the stomatal response to water stress, we get

$$g_s^{Et} = g_{max}^{Et} \eta(W) \alpha_1 B \quad (2.32)$$

where g_{max}^{Et} is the maximum stomatal conductance per unit of leaf area, and α_1 is the amount of leaf area per unit biomass [20].

A last addition to the surface processes and moisture fluxes is the addition of the sea water evaporating technology. It is assumed that this technology evaporates water in the same way as soil and vegetation (Figure 2.5), but with a very high surface conductance g_{ET}^E to optimize the LHF (Equation 2.30). The evaporation rate (E_{ET}) can then be calculated from the latent heat flux by

$$E_{ET} = \frac{LHF_{ET}}{\lambda\rho_{H_2O}} \quad (2.33)$$

and the total surface latent heat mass flux now combines to

$$\overline{(q'\omega')_s} = E_t + E_s + E_{ET} \quad (2.34)$$

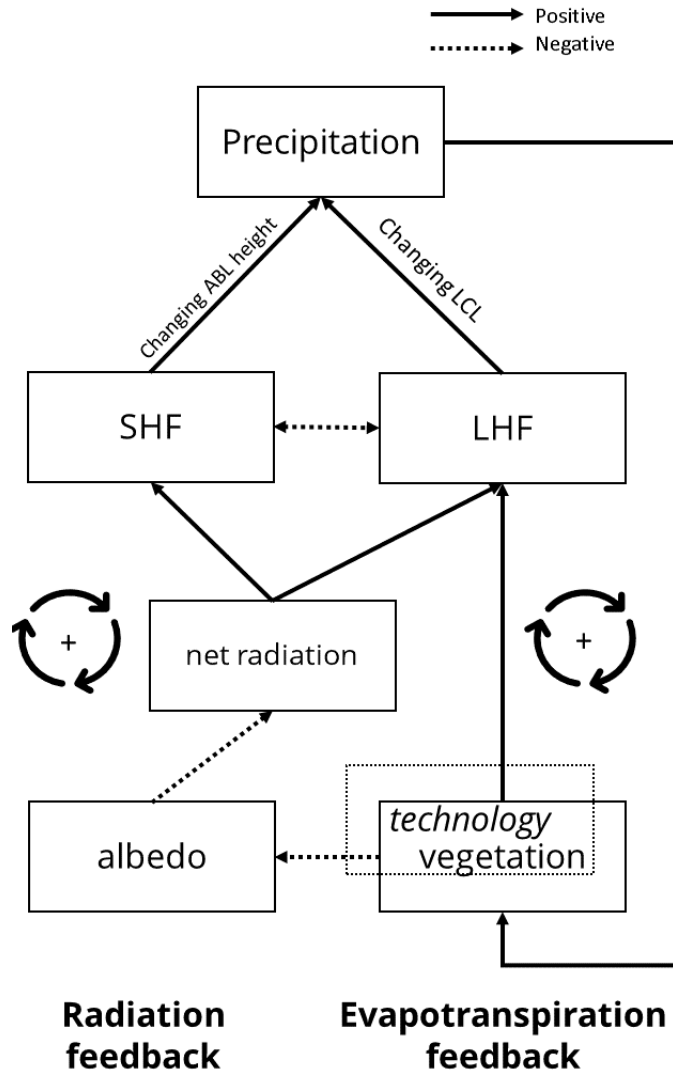


Figure 2.5: Adapted from Konings et al. [20]. Two parts of the macro-scale hydrological feedback related to vegetation as described in Section 2.1, with the addition of the sea water evaporating technology. The goal of the technology is to decrease the surface albedo and increase the latent heat flux to enhance precipitation.

3 | Methods

3.1 Model

The ABL model is defined on a one-dimensional vertical grid with a height of 5 km and step size $dz = 5$ m. The surface model is zero-dimensional. The coupled model is integrated in time using the Euler forward integration scheme with time step $dt = 60$ s. The air density is assumed to be constant throughout the ABL as required by the ABL slab model theory [35].

The model has two regimes: there are the nocturnal processes, such as the growth of the NBL, and the processes during the day, the growth of the CBL. To determine if it is day or night, one can look at the SHF and the R_n . When $SHF > 0$, there is turbulent heating of the ABL, so a convective layer can form. When $SHF \leq 0$, the turbulence decays, and a stable layer forms. Because SHF can be very small in some cases with high evaporation rates, we determine that it is daytime when $SHF + R_n > 0$ and nighttime when $SHF + R_n \leq 0$, which counteracts the switching to the nighttime regime in the middle of the afternoon in these cases.

The coupling between the surface and the ABL model is in the form of longwave radiation, sensible and latent (mass) heat fluxes and precipitation. For the moisture related variables, a conversion factor is needed to express the values in the right units: Moisture fluxes leaving and entering the subsurface water need to be multiplied by ρ_{air}/ρ_{H_2O} to convert from the units $[\text{m kg}_{H_2O} \text{ kg}_{air}^{-1} \text{ s}^{-1}]$ to $[\text{m s}^{-1}]$.

An overview of all variables, parameters, and constants used in this model is given in Appendix A.

3.1.1 Surface model

A radiation balance as described in Section 2.2 is used. Following a simple parameterization proposed by Stull [35], the ground heat flux is $G = 0.1R_n$ for $R_n > 0$ and $G = 0.5R_n$ for $R_n < 0$. The calculation of the surface radiative fluxes is looped until there is convergence, i.e. the difference in value before and after a new calculation is smaller than 10^{-5} W m^{-2} . The biomass and subsurface dynamics are as described in Section 2.5, with the addition that if the subsurface water is less than the wilting point (W_{wilt}), biomass evaporation becomes zero.

3.1.2 Atmospheric column model

In the morning, the CBL is initialized with a height of 5 m ($= dz$). The dynamics of the CBL are described by Equations 2.9, 2.10, 2.12, and 2.14. These equations

form a set of 4 equations with 5 unknowns, when γ_θ , $\overline{(\theta'\omega')_s}$, and w_L are specified as boundary conditions and it is assumed that there are no active clouds present and that there is no subsidence. The following closure assumption is made, directly relating $\overline{(\theta'\omega')_h}$ to the buoyancy flux at the surface:

$$\frac{-\overline{(\theta'\omega')_h}}{\overline{(\theta'\omega')_s}} = A_R \quad (3.1)$$

where A_R is assumed to be 0.2 [35]. This assumption is only used to determine the growth rate of the CBL; changes in θ due to entrainment are implicitly modelled by mixing the temperature of the column of air below the new CBL height after each integration time step.

The condensation and evaporation of liquid cloud droplets and the formation of rain water and rain is modelled as described in Section 2.4. The precipitation rate is calculated by assuming the rain water droplets precipitate out of the atmosphere with a constant rate (r_P). Integrating over the whole column of air gives:

$$P = r_P \int_{z=0}^{z=h} q_R dz \quad (3.2)$$

where it is assumed that $r_P = 0.001 \text{ s}^{-1}$.

Condensation and evaporation affect the potential temperature. From the condensation or evaporation flux the amount of sensible heat produced or consumed is calculated as follows:

$$Q_{\text{evap,cond}} = \frac{(C - E_c)\lambda}{c_p} \quad (3.3)$$

In the model this heat is added to the grid cell where the condensation or evaporation takes place, and only mixes when this grid cell is inside the CBL or gets entrained into the CBL.

The growth rate of the CBL is partially determined by the local value of $d\theta/dz = \gamma_\theta$ just above the CBL. This works well during growth through the NBL and through the free atmosphere, because those layers have stable temperature profiles. The residual layer on the other hand can have a neutral potential temperature profile, when radiative cooling is constant through the layer, and there is no advection of air into the layer. A neutral profile ($\gamma_\theta = 0$) would cause the CBL to grow infinitely fast through it. An artificial value $\gamma_{\theta,RL}$ is introduced to prevent this, which has to be tuned to obtain the desired behaviour.

The residual layer is modelled as follows: When it is night, the CBL height is set to 0, but all properties (height, temperature, and humidity) of this layer are transferred to the residual layer, which is assumed to not change, except when it gets entrained by the NBL during the night, or the CBL during the day. Radiative cooling in the residual layer is assumed to be constant (0.1 K hour^{-1} [35]) or is neglected when there is advection.

The dynamics of the NBL are modelled using Equation 2.18. The potential temperature profile is described by Equations 2.15 and 2.16 where the total heat flux acting on the bulk NBL (Q_T) is assumed to consist of the turbulent heat mass flux ($\overline{(\theta'\omega')_s}$), $Q_{\text{evap,cond}}$ in the NBL, and Q_R . Every timestep, moisture from evapotranspiration that is added to the NBL is evenly distributed through the layer.

At night, the NBL has to be initialized with a certain height, which is chosen to be 50 m. It is not lower (e.g. $dz = 5 \text{ m}$) because of probable undesirable behaviour

of the model: In the case of relatively high evaporation rates, the thin NBL becomes very moist, which causes the LHF to decrease. This in turn can cause the SHF to increase such that it switches sign. This mechanism can cause the model to rapidly change between the “day” and “night” regimes. This model behaviour can be counteracted by initializing the NBL with a greater initial height.

3.1.3 Boundary processes

Advection

Advection is an important dynamic process affecting the thermodynamics of ABL air masses [24]. In the current one column representation of the modelled system, advection can be included by adding an advection term to the local change equations. This advection term in one horizontal dimension would traditionally be in the form $U \frac{dX}{dx}$ where U represents the wind speed and $\frac{dX}{dx}$ is the local horizontal gradient of a certain variable X .

For a model where there is no explicitly modelled horizontal component, advection is a boundary condition. $\frac{dX}{dx} = \frac{\Delta X}{\Delta x}$ where $\Delta X = X_{\text{column model}} - X_{\text{upwind boundary}}$ and Δx is the assumed horizontal extent of the modelled column. The total change in a certain variable X can then be formulated as

$$\frac{dX}{dt} = \frac{\partial X}{\partial t} + U \frac{\Delta X}{\Delta x} \quad (3.4)$$

where X can be θ , q , q_L , or q_R . A distinction can be made between the wind speed during the day (U_{day}) and the wind speed during the night (U_{night}).

Orographic precipitation

The most familiar instance of orographic precipitation is where a mountain range lies across the prevailing wind direction: forced ascend up the windward slopes cools the air column (adiabatic cooling, see Equation B.5) [28]. The saturation vapor pressure of the atmosphere decreases exponentially with temperature, and hence with height [14], leading to saturation and enhanced precipitation when an air column undergoes forced ascend up a windward slope [28].

The simplest way of including orographic precipitation is by assuming that a fraction of the moisture leaving the modelled column through advection is advected over a mountain range and precipitates out at the windward side and through surface or groundwater flow acts as a source of subsurface water. This source term can then be added to Equation 2.27 which then becomes

$$\frac{dW}{dt} = P - E_t - E_s - r_w W + f_{\text{return}} U \frac{q + q_L + q_R}{\Delta x} \quad (3.5)$$

where f_{return} is the fraction of the atmospheric water leaving the column through advection that returns to the system as subsurface water by means of the processes described above. The time delay in atmospheric water leaving the system and flowing back into the system as subsurface water is neglected in this parameterization.

3.1.4 *Open, closed, and moving column modes*

Different model modes are used for different types of analysis and in general to gain a broader understanding of the model behaviour. The model is considered *open* when there is advection of atmospheric air and in and outflow of soil water, e.g. there is inflow and outflow of moisture in the system (OM, Table 3.1). This mode is used for sensitivity analysis and for the case studies.

The model is considered *closed* if there is no in and outflow of moisture. This is the case without advection, soil water inflow, or deep soil drainage. The assumption of a closed system allows us to look at what determines the distribution of moisture between the soil and the atmosphere. When we look at the equation of soil water (eq 2.27) it follows that in equilibrium

$$\frac{dW}{dt} = 0 \quad (3.6)$$

$$P = E_t + E_s \quad (3.7)$$

so that the precipitation to evapotranspiration ratio $\psi = 1$.

In a closed system where $B > 0$, we can see that when in equilibrium, the biomass equations (Equations 2.25 and 2.26) constrain the amount of soil water in the system:

$$\frac{dB}{dt} = 0 \quad (3.8)$$

$$b B \eta(W) - d_1 B = 0 \quad (3.9)$$

$$\eta(W) = \frac{d_1}{b} \quad (3.10)$$

$$\frac{W - W_{wilt}}{W^* - W_{wilt}} = \frac{d_1}{b} \quad (3.11)$$

$$W = \frac{d_1}{b}(W^* - W_{wilt}) + W_{wilt} \quad (3.12)$$

for $W_{wilt} < W < W^*$ and $B \neq 0$.

In this closed mode (CM1, Table 3.1), the model is not constrained by any boundary conditions, only by the initial amount of moisture in the system. The radiative budget of the model relies on parameterization (see Sections 2.3.2 and 3.1.2) instead of a radiation transfer model, which can lead to unrealistic warming or cooling of the modeled system. Therefore, an option that will be considered is the constraining of the atmospheric temperature to a certain profile (CM2, Table 3.1). This is done by adding an advection term (Equation 3.4) to the potential temperature equation (Equation B.5) during the night.

The last mode is the moving column mode (MCM, Table 3.1), which is in essence the same as the closed model mode, but with changing surface conditions, i.e. a column of air is assumed to be advected over a certain terrain (e.g. from the coast inland and up a mountain). This mode is used for the case study, and will not be run until equilibrium, but as long as it takes to travel the path.

The path is chosen along a streamline and the velocity along this streamline is assumed to be constant in time and space. The surface component of the model is constant in time but not in space. Variables that have to be known along the streamline in the MCM are surface pressure, subsurface water, and latitude. The evaporation technology can be added anywhere along the path.

Table 3.1: Descriptions of the different modes of the model used in this research including the relevant research questions (RQ) as described in Chapter 1 Introduction.

Model code	Description	Use
OM	Open model	Sensitivity analysis, case studies. RQ 1, 2, and 4.
OMT	Open model with evaporation through technology for the whole model run	Sensitivity analysis, case studies. RQ 2 and 4.
CM1	Closed model, unconstrained atmospheric temperature	Sensitivity analysis (initial conditions). RQ 1.
CM2	Closed model, partly constrained atmospheric temperature	Sensitivity analysis (initial conditions). RQ 1.
MCM	Moving column mode	Case studies. RQ 4.

3.2 Sensitivity analysis

A sensitivity analysis will be done to determine the relative importance of the different variables and model choices on the amount of precipitation, soil water, and vegetation in the OM, CM1, and CM2 modes. Then a second sensitivity analysis will be done in the OMT mode to determine the conditions under which enhanced evaporation through technology can be effective. Here, also the parameters affecting the technology itself will be varied, to try to find what the optimal properties of the technology would be.

The reference point is mid spring (April 20) 35°N with a typical temperature profile of this latitude at this time of the year where $\gamma_\theta = 5$ K/km and $\phi_\theta = 300$ K. For the atmosphere, the specific humidity is assumed to be constant with height [11], up to 4000 m and $\phi_q = 6$ g kg⁻¹. To prevent large scale precipitation in the OM and OMT modes, if $q > q_{sat}$ for certain heights for the boundary profile, $q = q_{sat}$ for these heights. The starting value for the soil moisture is 10% of the soil moisture capacity. An overview of all reference parameter values is given in Appendix A.

For the technology, the reference point is that the technology covers 50% of the surface (technology fraction = 0.5), has a surface conductance of 0.01 m s⁻¹, and an albedo of 0.1. In OMT mode, the surface model is divided in two separate parts, according to the technology fraction, that both have their own energy balance.

3.3 Case studies

3.3.1 Case study selection

A combination of criteria is chosen to find suitable case study regions: the subsurface water content, the specific humidity near the surface and the near surface temperature. To this end, the ERA5 monthly averaged data on single levels from

1979 to present of surface pressure, 2m temperature, 2m dewpoint temperature, and volumetric soil water layer 1 and 2 for the year of 2021 is used, and averaged over the year to get one value per grid cell. Thresholds are implemented to find regions that have a dry soil, are not too hot throughout the year and have a relatively moist atmosphere. The thresholds are tuned to obtain regions in both the northern and the southern hemisphere (Table 3.2). From the regions that meet the criteria, one is chosen as a case study region. From that region, three case study locations are chosen.

Table 3.2: Variable thresholds in the northern and the southern hemisphere used for the selection of case study regions.

Variable	Threshold	
	NH	SH
W up to 28 cm deep	< 10 cm	< 15 cm
2m q	> 0.006 kg/kg	> 0.006 kg/kg
2m T_{air}	< 295 K	< 292 K

3.3.2 Data and parameter tuning

For the chosen case study region, the month is chosen that shows highest 2m specific humidity and lowest 2m temperature in 2021. For the three case study locations, ERA5 reanalysis data are used to tune the model to these locations (Appendix B.2). The choice of data was restricted to reanalysis data because there was no data available from weather stations and radiosondes.

As boundary conditions ERA5 monthly averaged data on pressure levels, reanalysis by hour of the day of temperature, specific humidity, and the U and V components of the wind are used [12]. Thus, in contrast to other OM and OMT mode runs, OM and OMT mode case study runs have hourly varying boundary conditions. The profiles are interpolated to match the vertical grid of the model.

The radiative fluxes at the surface are tuned by varying the fraction of net radiation that is the ground heat flux for $R_n > 0$ (Section 3.1.1), the aerodynamic resistance, and the maximum surface conductance. The surface temperature and the 2m temperature are tuned by varying the NBL scaling time, the NBL equilibrium height, and the aerodynamic resistance (Table 3.3). The model has one day of run up time and then the model is tuned for the second model day. The coefficient of determination (R^2) is calculated to help finding the best parameter values. For the runs in MCM, average parameter values of the three locations are used for the whole run (Table 3.3).

N.B. The ERA5 monthly averaged data used of radiative and turbulent fluxes had missing data points for hours 2-8.

3.3.3 Model runs

Open model

For the case study runs in OM and OMT modes ERA5 monthly averaged reanalysis data by hour of day on pressure levels is interpolated to have hourly varying

Table 3.3: Tuning parameter values for the case study locations, with the standard value used in this research for comparison. The mean of the three case study locations used for the runs in moving column mode (MCM). τ 7 hours and $h_{eq} = 500$ m are the minimum and maximum values of their respective normal range of values [35].

Variable	Standard	Case study location			MCM
		Sinai 1	Sinai 2	Sinai 3	
Ground flux fraction	0.1	0.4	0.4	0.35	0.38
r_a (s m ⁻¹)	50	75	75	75	75
g_{max}^{Es} (m s ⁻¹)	0.0005	0.001	0.0001	0.00015	0.0042
τ (hours)	13.5	7	7	7	7
h_{eq} (m)	300	500	500	400	467
W^* (cm)	1.93	5.79	5.79	5.79	5.79

boundary conditions of wind speed, potential temperature, and specific humidity [12]. The model is run for 100 days to ensure an equilibrium (daily limit cycle) is reached. The water fluxes in the system are then compared to the runs with and without technology.

Moving column

The model is also run for the case study region in MCM as described in Section 3.1.4. The mean of the 10m wind in one direction over the whole streamline is used as the moving speed of the column. At the start of the path, the surface is assumed to be completely covered by the technology for 10 km. ERA5 reanalysis data of surface pressure and subsurface water are interpolated to diminish any sudden jumps in surface conditions. The changes in height are manifested in the change in surface pressure along the streamline. The model has a run up time of 1 day and 9 hours before it starts moving to ensure that the evaporation technology covered surface is passed in daytime.

Variables that have to be known along the streamline in the MCM are surface pressure, subsurface water, vegetation biomass, albedo, and latitude. For the case study done in this research, the vegetation biomass along the streamline was negligible and the reanalysis albedo was approximately equal to 0.4 which agrees with the previously defined α_{max} : the albedo of surface without vegetation.

4 | Results

4.1 Sensitivity analysis of model equilibria

4.1.1 Introduction

In this section the results are presented for the sensitivity analysis and general model behaviour in CM1, CM2, and OM modes (Table 3.1). The CM modes have a fixed amount of moisture in the system, i.e. there is no moisture exchange with the environment. CM2 mode has a constrained atmospheric temperature meaning that at night the temperature will go towards a predefined temperature profile, as if there was advection of temperature only.

4.1.2 Closed model modes

A sensitivity analysis for different initial moisture and temperature profiles in CM1 mode show that the subsurface water level goes towards the equilibrium¹ value found from Equation 3.8, with the exception of the case where the initial atmosphere is completely dry (Figure 4.1a). For this initial dry atmosphere, higher subsurface water levels are found, with the amount increasing with the initial temperature. When looking at biomass (Figure 4.1c), it can be seen that ϕ_q determines the result, where a lower ϕ_q results in more vegetation and $\phi_q = 0$ results in maximum vegetation. These counter-intuitive results cannot be explained from the albedo feedback (Figure C.5), and they will be shortly discussed in Section 5.2.

As explained in the methods section, allowing the model to go towards the equilibrium determined by Equation 3.8 results in very high temperatures (up to 334 K, Figure C.6a) that are needed to move the subsurface water towards the atmosphere and keep the bulk of the moisture in the atmosphere instead of in the soil for high ϕ_q . Constraining the atmospheric temperature leads to different and more intuitive results: For cold (warm) and moist (dry) atmospheres, vegetation goes towards its maximum (minimum) value (Figure 4.1d).

In the intermediate atmospheres, it is found that the subsurface water goes towards or near the equilibrium found from Equation 3.8 (Figure 4.1b), and that the amount of vegetation seems to positively relate to the amount of subsurface water. The maximum surface temperatures found are now indeed less extreme than for the unconstrained model, and are mostly determined by ϕ_θ (Figure C.6b). However, the initial ϕ_q also has an effect on the temperatures, where higher ϕ_q seems to relate to

¹The equilibrium is a daily limit cycle. The values discussed are the last values of the model run (end of the day at midnight), with the exception of the surface temperatures and CBL height where the minimum and/or maximum values of the last model day are used.

lower maximum surface temperatures, with two outliers for $\phi_q = 0$ and $\phi_\theta = 300$ or 305 K. Here, an equilibrium forms where there is virtually no precipitation and evaporation and $W = 0$ cm. The results are summarized in Table 4.1.

Table 4.1: Results of the sensitivity analysis in CM1 and CM2 modes. The impact on precipitation P , subsurface water W , and vegetation biomass B is shown indicated by symbols and colors. 0: no impact. +/- and green/red color: positive/negative impact.

Parameter	Tested range	P	W	B	Figure
CM1 mode section 4.1.2					
B (ini)	0 - 1 kg m ⁻²	0*	0*	0*	C.1
W (ini)	0 - 0.04 m	0 [†]	0 or + [†]	0 or - [†]	C.2
ϕ_θ (ini)	285 - 305 K, for ϕ_q (ini) $\neq 0$ kg kg ⁻¹	0	0	0	4.1a 4.1c
	285 - 305 K, for ϕ_q (ini) = 0 kg kg ⁻¹	-	+	0	
ϕ_q (ini)	0 - 12 · 10 ⁻³ kg kg ⁻¹	0 or + [‡]	0 or + [‡]	0 or - [‡]	4.1a 4.1c
CM2 mode section 4.1.2					
B (ini)	0 - 1 kg m ⁻²	0*	0*	0*	C.3
W (ini)	0 - 0.5 m	0 or +	0 or +	0 or +	C.4
ϕ_θ	285 - 305 K	- [§]	-	0 or -	4.1b 4.1d
ϕ_q (ini)	0 - 12 · 10 ⁻³ kg kg ⁻¹	+	+	0 or +	4.1b 4.1d
*Except where B (ini) = 0.					
[†] For some values, no equilibrium was reached depending on ϕ_q (ini). These values are not considered when determining the impact.					
[‡] For some values, no equilibrium was reached depending on ϕ_q (ini).					
[§] This trend is broken for ϕ_q (ini) ≥ 0.009 kg kg ⁻¹ and $\phi_\theta = 285$ K.					

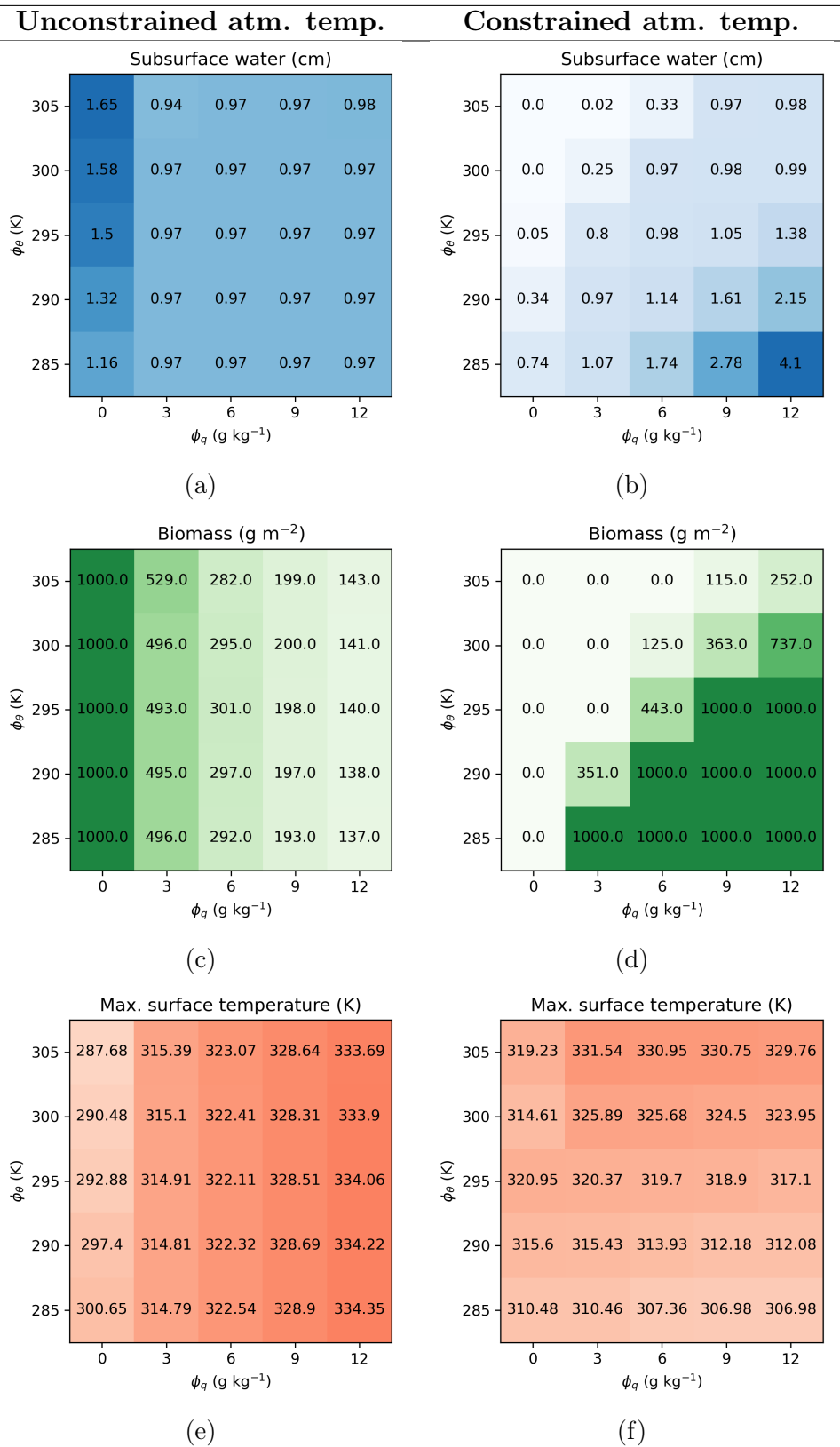


Figure 4.1: Closed model (CM) sensitivity results for varying the atmospheric moisture and atmospheric temperature parameters of the initial conditions. Results for subsurface water (first row), vegetation biomass (second row), and the maximum surface temperature (third row) for the unconstrained (CM1, left column) and constrained atmospheric temperatures (CM2, right column) are shown.

4.1.3 Open model mode

In OM mode, a sensitivity analysis is done for initial conditions, boundary conditions, and twelve other parameters. All results are summarized in Table 4.2. The most important results are discussed below. Other results are shown in Appendix C.

For the OM mode, the patterns found for the different atmospheric moisture and temperature profiles are comparable to the results from the CM2 mode: higher amounts of subsurface water, precipitation and biomass are found for colder and moister atmospheres (Figures 4.2a-c). However, there are significant differences in the equilibrium surface water, where the equilibrium amounts are overall lower for the OM mode than for the CM2 mode. The range of atmospheric profiles that result in vegetation is also smaller. The specific humidity profile for the most part determines the total amount of water in the atmospheric column (Figure C.7). It can be seen that small amounts of atmospheric moisture do not result in the formation of precipitation (Figure 4.2a) and therefore cause an almost completely dry soil. Since there is an influx of water through the *orographic precipitation* flux the soil is only completely dry for $\phi_q = 0 \text{ g kg}^{-1}$.

The latitude and the time of the year determine the incoming solar radiation in the model. For all latitudes $> 0^\circ\text{N}$ a positive effect of the day of the year on the CBL height is visible which can be related to the total amount of incoming radiation per day (Figure 4.2d). The largest change is visible when going from winter (Day of the year = 18) to spring (Day of the year = 109), and this difference increases with latitude. It is even found that the model does not work for latitudes $\geq 45^\circ\text{N}$ in winter, because the amount of incoming radiation is not enough for a CBL to form. This shows that for higher latitudes in winter the low amount of incoming solar radiation has a large role in the limitation of the CBL height.

Initial conditions for subsurface water and biomass have no effect on the limit cycle that the system goes to, with the exception of $B = 0$ which prevents biomass from growing at all. Other variables can have an effect on precipitation and subsurface water and these are summarized in Table 4.2 and shown in Appendix C.

4.1.4 Summary

The model shows different behaviour for the different model modes. In the CM1 mode, the model is mostly constrained by the subsurface water equilibrium value, which leads to counter-intuitive results for the vegetation biomass. The CM2 and OM modes show similar and more intuitive behaviour regarding the direction of the model equilibria, i.e. the maxima are found for the same parameter values. However, in the OM mode the amount of water in the system is not determined by the initial conditions and it is found that the equilibria are overall dryer in the OM mode than in the CM2 mode. The amount of subsurface water, precipitation, and vegetation in OM mode is mostly determined by the boundary conditions, i.e. the atmospheric profiles of temperature and specific humidity. Latitude and day of the year play an important part in determining the atmospheric boundary layer height by constraining the amount of incoming shortwave radiation.

Table 4.2: Results of the sensitivity analysis in OM mode. The impact on precipitation P , subsurface water W , and vegetation biomass B is shown indicated by symbols and colors. 0: no impact. +/- and green/red color: positive/negative impact. max and yellow color: there is a maximum found for an intermediate value of the tested range.

Parameter	Tested range	P	W	B	Figure
OM mode					
B (ini)	0 - 1 kg m ⁻²	0*	0*	0*	
W (ini)	0 - 0.5 m	0	0	0	
ϕ_θ	285 - 305 K	-	-	-	4.2
ϕ_q	0 - 12 · 10 ⁻³ kgkg ⁻¹	+	+	+	4.2
D	18 - 200	+ [†]	+ [†]	0	4.2
ϕ	0 - 45 degrees N, winter	0 or -	0	0	4.2
	0 - 45 degrees N, autumn/spring	max	max	0	
	0 - 45 degrees N, summer	max	+	0	
h_{eq}	100 - 500 m	-	-	0	C.8
τ	7 - 30 hours	+	+	0	C.8
g_{max}^{Es}	0.0005 - 0.01 m s ⁻¹	0	0	0	C.9
g_{max}^{Et}	0.0005 - 0.01 m s ⁻¹	0	0	0	C.9
r_a	1 - 75 s m ⁻¹	-	-	0	C.10
ρ_{air}	0.6 - 1.2 kg m ⁻³	0 or +	0 or +	0	C.11
		+	+		
A	0.1 - 0.3	-	-	0	C.12
U_{day}	0 - 5 m s ⁻¹	+	+	0	C.13
U_{night}	0 - 5 m s ⁻¹	+	+	0	C.13

*Except where B (ini) = 0.

[†]Except at the equator. Then the highest value is found in Spring.

[‡]This negative relationship only holds as long as $B_{max} >$ the equilibrium value of B .

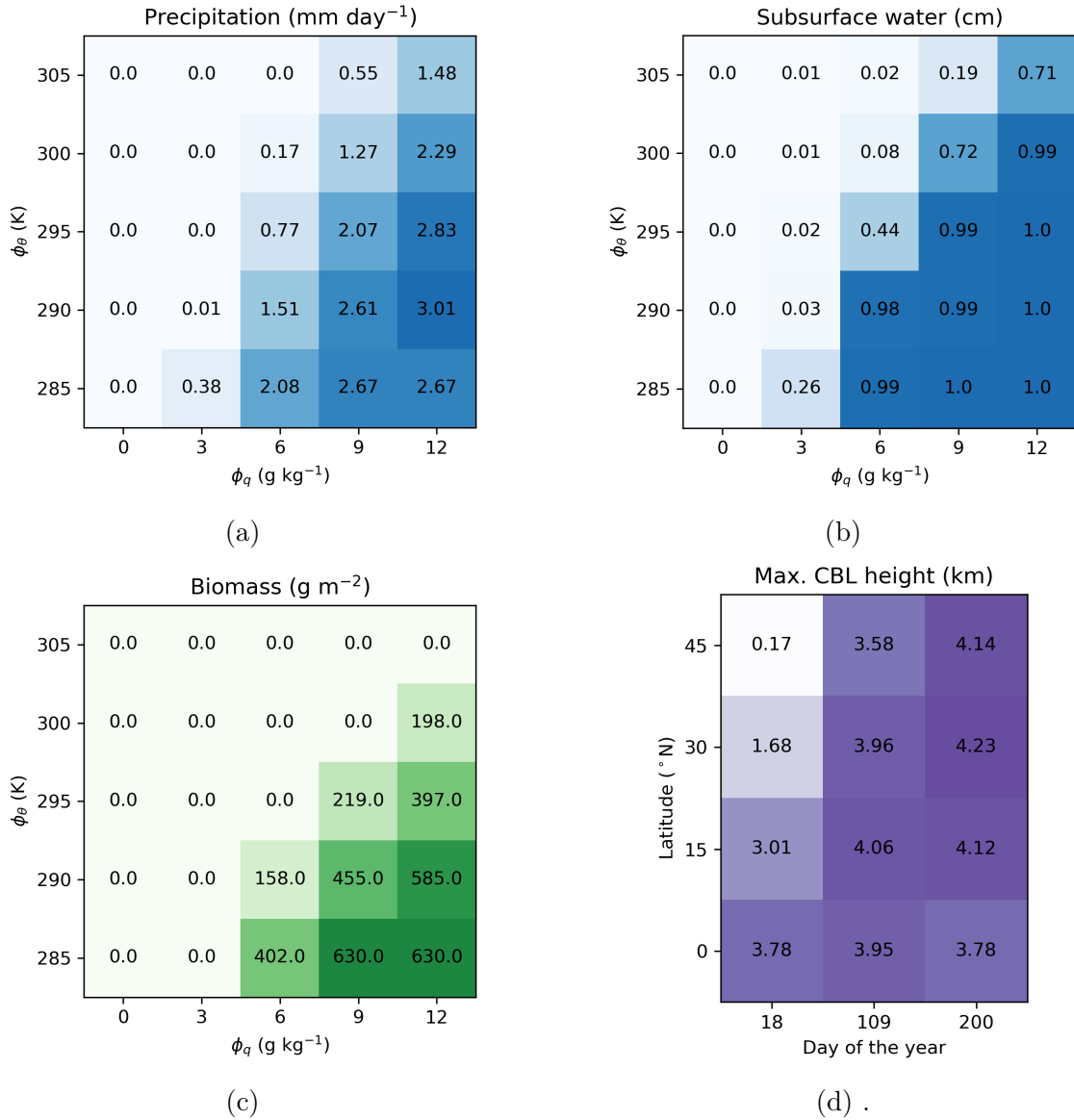


Figure 4.2: Open model (OM) sensitivity results for varying atmospheric moisture and atmospheric temperature parameters (a-c) and varying latitude and day of the year (d). In panel d, the days of the year correspond from low to high to winter, spring, and summer. Autumn is not shown because it is assumed to yield the same result as spring, because only the incoming solar radiation is varied.

4.2 The effect of enhanced evaporation through technology

4.2.1 Introduction

The results of the sensitivity analysis of the evaporation technology parameters are presented first to determine for which parameters the technology could be the most effective. Then, the results in OM mode from the previous section are compared to the results in OMT mode. Since it was found in the previous section that initial conditions do not affect the equilibrium results in OM mode, the evaporation technology is turned on for the complete duration of the runs. Results are summarized in Table 4.3.

4.2.2 Sensitivity to the technology's variables

Varying the fraction of the surface that the technology occupies shows that for all specific humidity profiles, the technology inhibits precipitation formation (Figure 4.3a). However, for high surface fractions (> 0.5) the amount of precipitation increases with the surface fraction occupied by the technology. For different temperature profiles, a similar result is found with maxima in precipitation for the case without the evaporation technology, and maxima for the case where almost all surface is occupied by the technology (Figure 4.3b). Here, the technology does have a positive impact on the amount of precipitation when the fraction is high enough. Lastly it can be seen that there is a threshold temperature profile of $295 \text{ K} < \phi_\theta < 300 \text{ K}$ from where on the technology does only have a negative effect on the amount of precipitation.

Now looking at the subsurface water, it can be observed that for both the different specific humidity (Figure 4.3c) and temperature profiles (Figure 4.3d), the technology can have a positive effect. This can be explained by the reduced water loss from the soil due to inhibited evaporation where the technology provides shading. For the different specific humidity profiles this positive effect is only found for very humid atmospheres and a surface fraction of the technology of 0.9. The vegetation biomass shows similar patterns as the subsurface water (Figure C.14).

The surface conductance of the technology affects the energy partitioning: for a higher conductance, more water will evaporate and the sensible heat flux will be lower. The case where the technology surface conductance is zero can be interpreted as covering part of the surface with a dark cloth which does not evaporate any water itself. Here it can be seen that a lower technology surface conductance will lead to more precipitation for most atmospheric profiles (figures 4.4a and 4.4b). This is because although higher conductance leads to a higher specific humidity in the column, it also decreases the SHF and inhibits the growth of the CBL. The increased precipitation resulting from a higher CBL is apparently more than the increased precipitation from an increased moisture content in the atmospheric column. The exception is for the driest cases ($\phi_q \leq 3 \text{ g kg}^{-1}$), where the highest surface conductance will lead to more precipitation. However, these precipitation amounts are of a negligible magnitude: The technology causes a precipitation increase from 0.0 to 0.04 or 0.05 mm day^{-1} .

The sensitivity of the system to the technology surface albedo shows the most

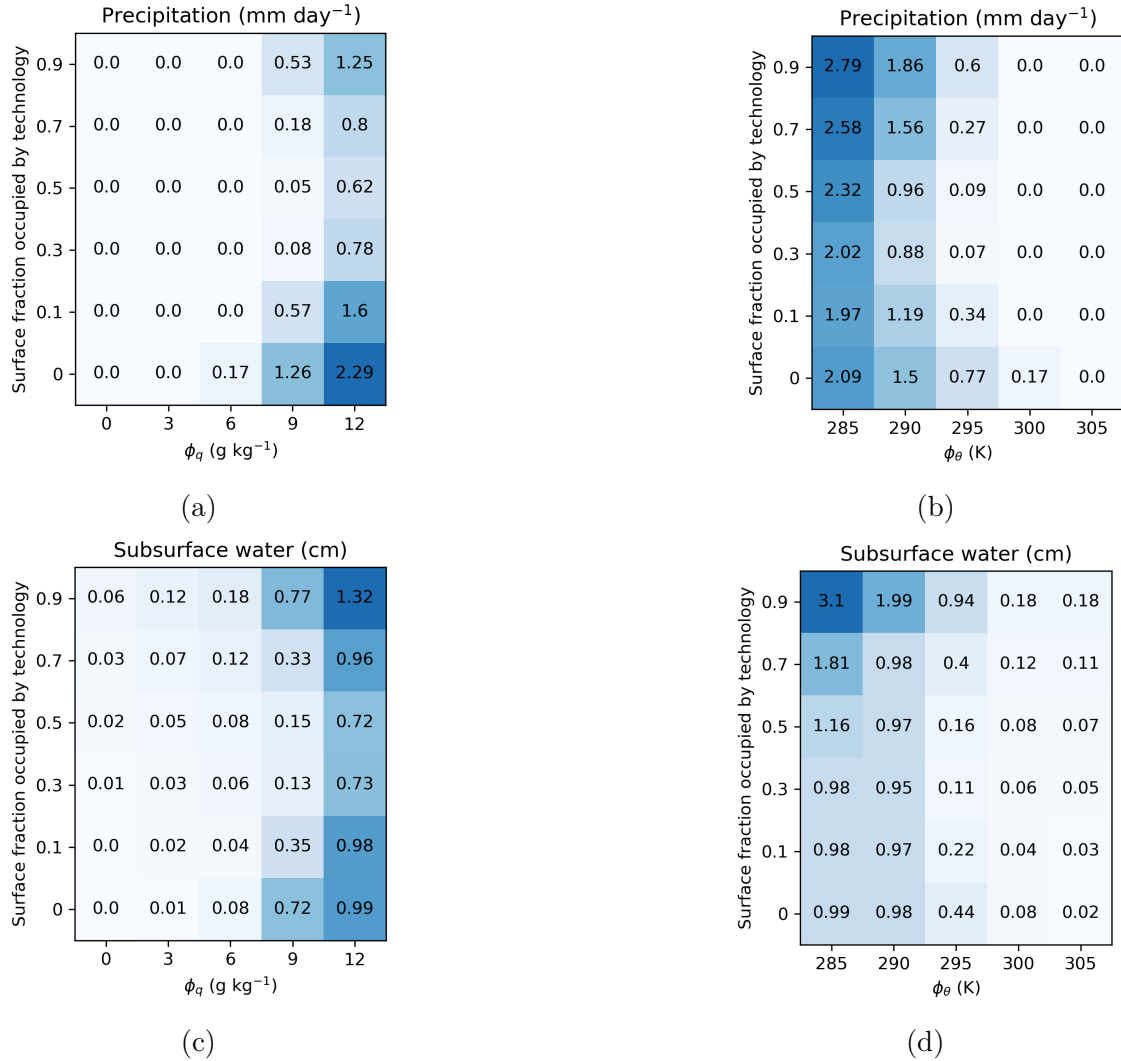


Figure 4.3: Open model with technology (OMT mode) sensitivity results for a varying surface fraction occupied by the technology. Surface fraction = 0 is equivalent to model runs in OM mode. Results for precipitation (top row) and subsurface water (bottom row) are shown. For the panels in the left column the boundary conditions for atmospheric specific humidity are varied and for the panels in the right column the boundary conditions for the atmospheric temperature are varied. Results for vegetation biomass are shown in Figure C.14.

Table 4.3: Results of the sensitivity analysis in OMT mode. The impact on precipitation P , subsurface water W , and vegetation biomass B is shown indicated by symbols and colors. 0: no impact. +/- and green/red color: positive/negative impact. min and yellow color: there is a minimum found for an intermediate value of the tested range.

Parameter	Tested range	P	W	B	Section
OMT mode					
Techno- logy fraction	0 - 0.9, for $\phi_q \geq 0.006 \text{ kg kg}^{-1}$	min	min	0 or min*	
	0 - 0.9, for $\phi_\theta \leq 300 \text{ K}$	min	min	+	
				min or 0†	
g_{ET}^E	0 - 0.05 m s^{-1}	-‡	-‡	-	
α_{ET}	0.1 - 0.9	0 or -	0 or -	0 or -	
<p>*Only min for $\phi_q \geq 0.012 \text{ kg kg}^{-1}$. †+ for $\phi_\theta = 285 \text{ K}$, min for $\phi_\theta = 290 \text{ K}$, and 0 for $\phi_\theta \geq 295 \text{ K}$. ‡Some exceptions exist where there is a slight increase in P and W for $g_{ET}^E > 0.01$.</p>					

straightforward result: A lower surface albedo leads to a higher amount of precipitation (Figures 4.4c and 4.4d). This is because of the increase in net radiation which will lead to both a higher SHF and a higher LHF , which both affect the amount of precipitation positively.

4.2.3 Summary

It was found that for the best results, as much surface as possible would need to be covered by the technology. With small amounts of surface coverage, the technology can have a negative effect, mostly on precipitation but also on subsurface water and vegetation. Also, it seems to work best to not evaporate any water, but to only lower the surface albedo. Since this contradicts the purpose of this research, the no evaporation case will not be used for further results. Two modes of the evaporation technology will be discussed: the low evaporation mode (OMTL) where $g_{ET}^E = 0.001$ and the high evaporation mode (OMTH) where $g_{ET}^E = 0.01$ (Table 4.4).

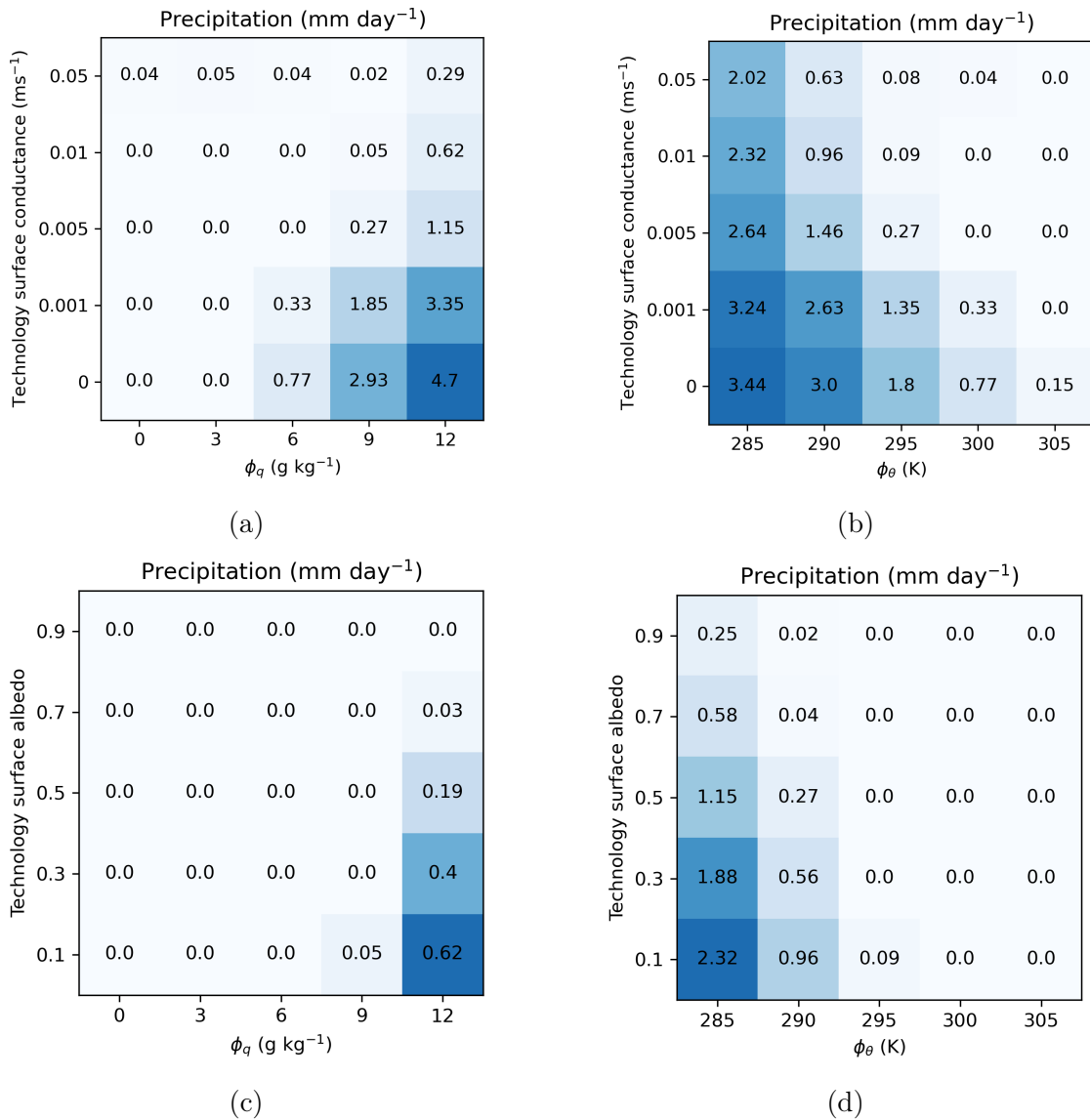


Figure 4.4: Open model with technology (OMT mode) sensitivity precipitation results for a varying technology surface conductance (top row) and a varying technology surface albedo (bottom row). Technology surface conductance = 0 ms^{-1} can be interpreted as covering the surface with a dark cloth that does not evaporate sea water. For the panels in the left column the boundary conditions for atmospheric specific humidity are varied and for the panels in the right column the boundary conditions for the atmospheric temperature are varied.

Table 4.4: Descriptions of the two modes of the sea water evaporation technology that are being investigated in Section 4.3.

Model code	Description	Values
OMTL	Low evaporation mode. The technology evaporates little seawater because of a low surface conductance, comparable to the max stomatal conductance.	fraction = 0.7 $g_{ET}^E = 0.001$ $\alpha = 0.1$
OMTH	High evaporation mode. The technology evaporates more seawater because of a ten times higher surface conductance than in OMTL mode.	fraction = 0.7 $g_{ET}^E = 0.01$ $\alpha = 0.1$

4.3 Regions where the evaporation technology can be effective

4.3.1 Introduction

In this section a sensitivity analysis is done where the evaporation technology is included in the model (OMTL and OMTH modes, Table 4.4) and the sensitivity is tested for different atmospheric boundary conditions. These results are then compared to the equivalent runs without the technology (OM mode, Section 4.1.3). The results of this analysis are then used to determine the regions where the technology could be effective, by plotting ERA5 reanalysis data.

4.3.2 Sensitivity analysis in OMTL and OMTH modes

OMTL sensitivity runs

The results of the sensitivity analysis in OMTL mode show a general trend where more moisture in the atmosphere leads to a larger positive impact of the technology on precipitation and subsurface water (Figure 4.5). For temperature, it can be seen that generally a lower temperature leads to a higher (increase in the) precipitation and subsurface water, except for the moistest atmospheres ($\phi_q \geq 6 \text{ g kg}^{-1}$), where there is an optimum around 290 or 295 K. This was also found for the model runs without technology (Figure 4.2a), however in the OMTL runs, this difference is also reflected in the subsurface water, where in the OM runs it was not (compare Figures 4.2b and 4.5c).

The results for vegetation show that the equilibrium of ten of the runs increased to the maximum amount of vegetation biomass in OMTL mode (Figure 4.5e). Furthermore, there are four runs where the model goes from no vegetation in OM mode, to vegetated in OMTL mode. This indicates that the low evaporating technology did not only enhance existing vegetation in the model, but also caused the subsurface water to pass a threshold causing the model to support vegetation growth. This threshold was passed for the combinations (ϕ_θ, ϕ_q) : (305 K, 12 g kg⁻¹), (300 K, 9 g kg⁻¹), (295 K, 6 g kg⁻¹), and (285 K, 3 g kg⁻¹). The cap on biomass can explain the pattern in vegetation biomass difference between the OM and OMTL runs where the maxima are found near the transition between vegetated and non-vegetated states (Figure 4.5f), i.e. the cap on biomass limits the potential growth of vegetation biomass which is mostly limiting for situations where the biomass was already near its maximum in OM mode.

OMTH sensitivity runs

Now continuing with the results of the sensitivity analysis in OMTH mode (Figure 4.6) it can be seen that the general trend is that for a colder atmosphere the technology is more effective in enhancing precipitation and subsurface water. For warmer atmospheres that are relatively moist the technology can even be suppressive for precipitation and subsurface water. The explanation can be found when considering that the increase in evaporation is at the expense of the sensible heat flux. The evaporation can increase more where the atmosphere is warmer (Equa-

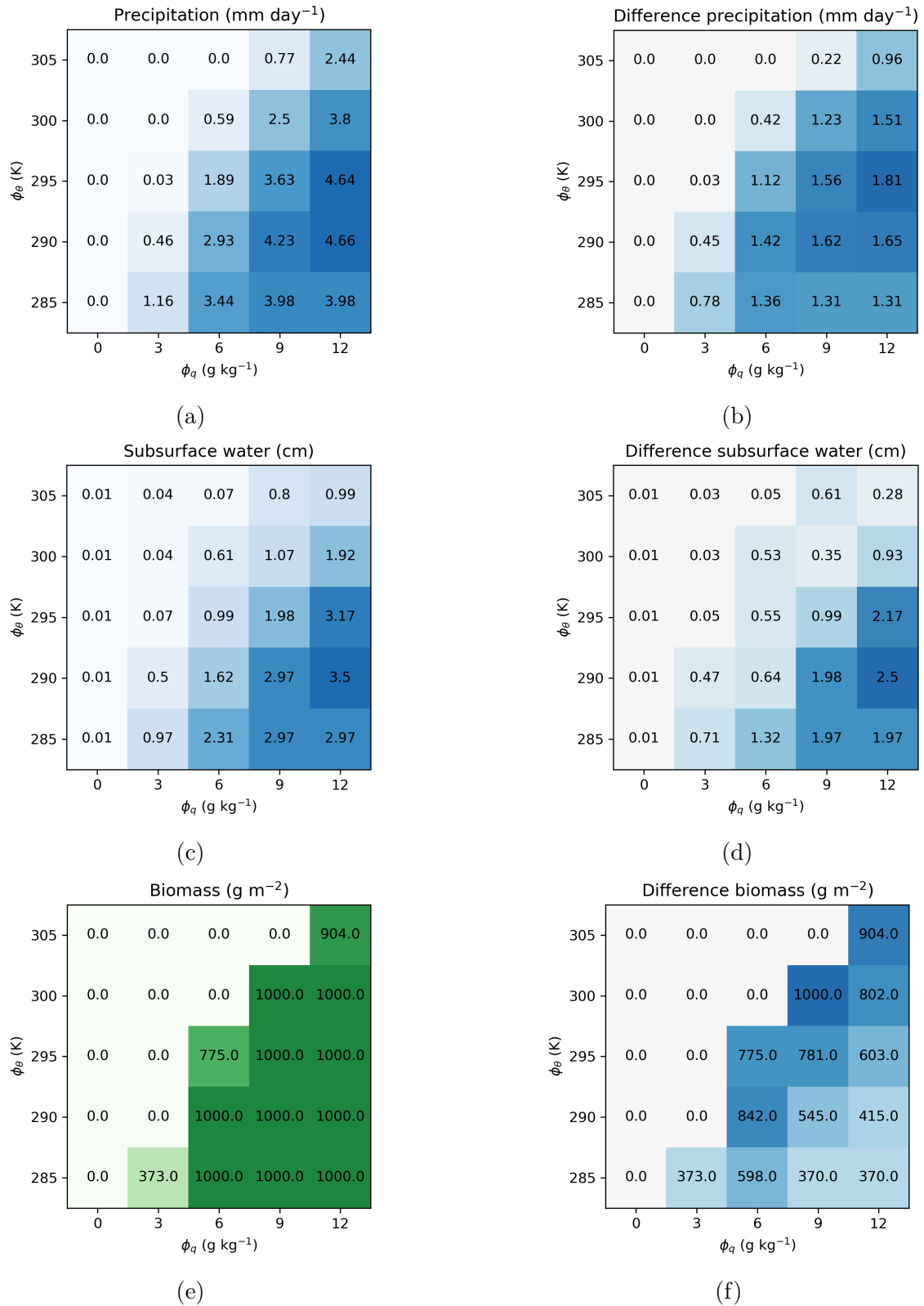


Figure 4.5: Panels a, c, e show the sensitivity of the system in OMTL mode to specific humidity and temperature parameters. Panels b, d, f show the difference between between OM mode and OMTL mode, e.g. the difference between figures 4.2a and 4.5a, 4.2b and 4.5c, and 4.2c and 4.5e respectively.

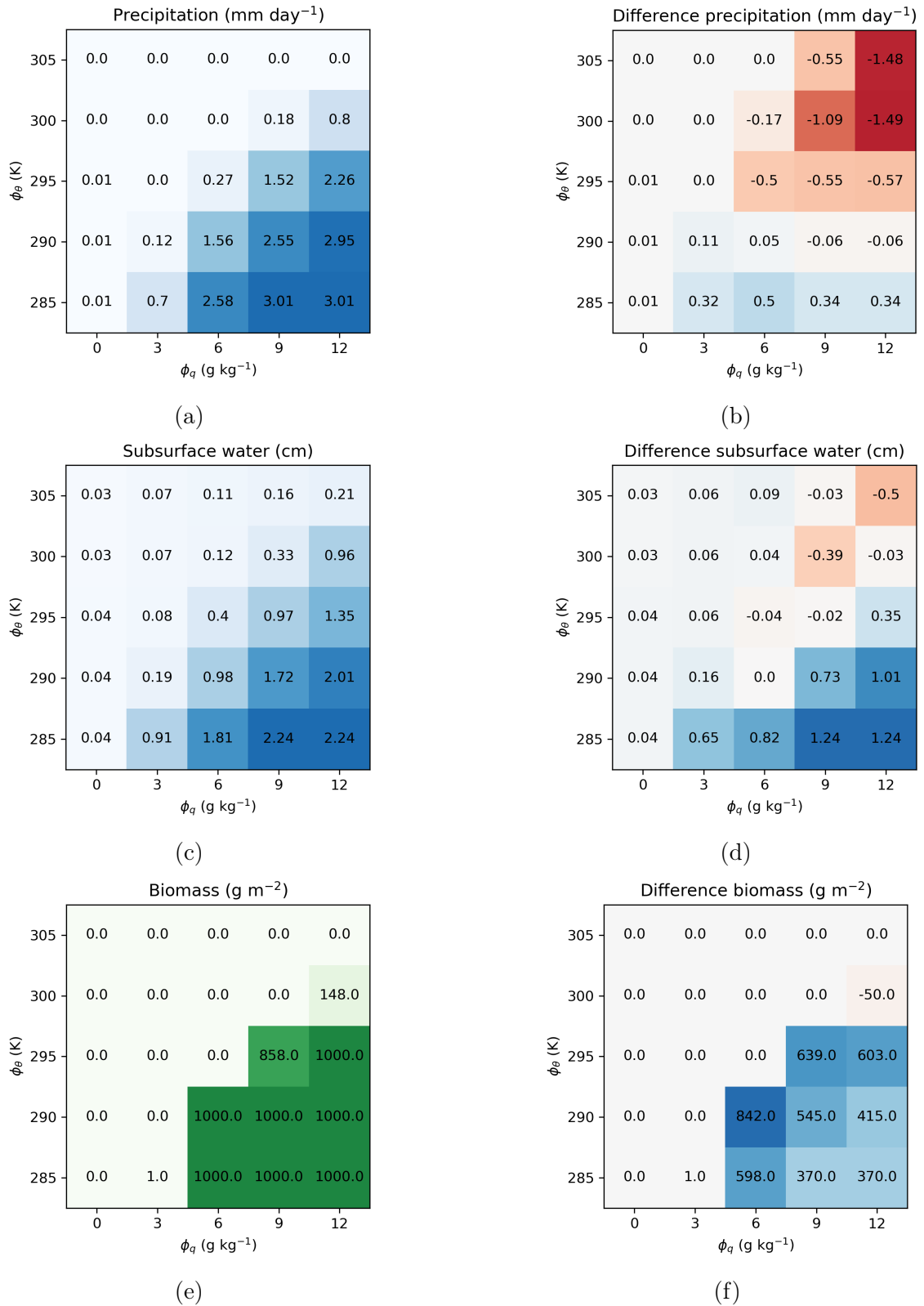


Figure 4.6: Panels a, c, e show the sensitivity of the system in OMTH mode to specific humidity and temperature parameters. Panels b, d, f show the difference between between OM mode and OMTH mode, e.g. the difference between figures 4.2a and 4.6a, 4.2b and 4.6c, and 4.2c and 4.6e respectively.

tion 2.30, Figure C.15a), which leads to a larger negative effect on the CBL height (Figure C.15b). Since in moist but warm atmospheres the occurrence of convective precipitation depends on the development of a high CBL, the repressive effect of the technology on the CBL height leads to a suppression of precipitation.

The results for vegetation show that the equilibrium of 7 of the runs is the maximum amount of vegetation biomass (Figure 4.6e). Furthermore, there are no model runs where the technology has switched the equilibrium from having no vegetation to a vegetated state (Figure 4.5f). There is one model run where the technology even inhibits vegetation growth.

Temperature effects

Besides the effects on precipitation, subsurface water, and vegetation, the technology also affects the temperature. Looking at the differences caused by the technology in OMTL mode for the minimum and maximum surface temperatures, it can be observed that the technology generally causes an increase in surface temperature with some exceptions for the warmest boundary conditions ($\phi_\theta \geq 300$ K) (Figure 4.7). A clear outlier in these results is the case of the completely dry atmosphere where the difference is extremely large (> 21 K). This result is caused by the definition of the incoming longwave radiation at the surface (Equations 2.2-2.4) and will be discussed later in Section 5.3. When ignoring the outlier, increases in temperature are generally higher for the maximum surface temperatures and show an increase with atmospheric moisture and a decrease with atmospheric temperature. The minimum surface temperatures do not show the same pattern but have maxima around some intermediate parameter values.

Now looking at the differences caused by the technology in OMTH mode for the minimum and maximum surface temperatures and ignoring the outliers for $\phi_q = 0$, it can be seen that the technology causes an increase in minimum surface temperature and a decrease in the maximum surface temperature, so generally making the daily range of temperatures smaller (Figure C.15). The maximum surface temperatures show the largest decrease where ϕ_θ is the highest.

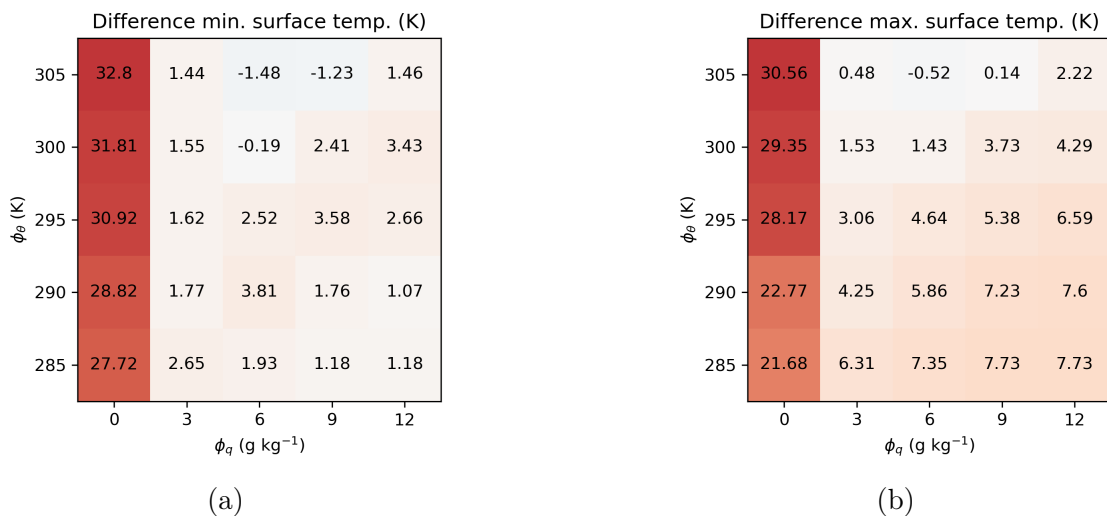


Figure 4.7: OMTL mode differences in daily surface temperature extremes compared to OM mode.

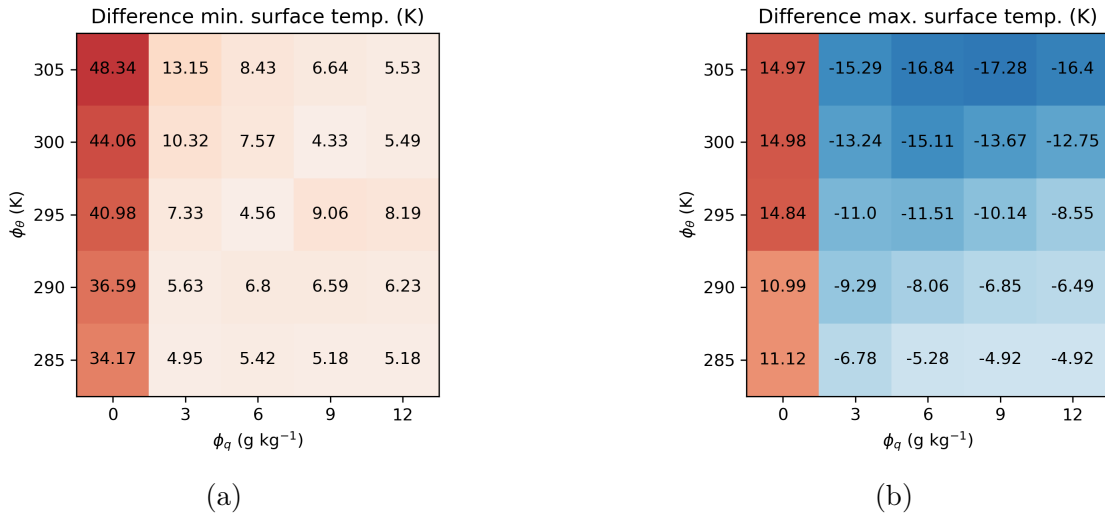


Figure 4.8: OMTM mode differences in daily surface temperature extremes compared to OM mode.

4.3.3 Where can the technology be effective?

ERA5 reanalysis data is used to find regions where the evaporation technology can potentially be effective according to the sensitivity analysis results from the previous section. From the sensitivity analysis it was found that for the technology to have a positive impact on precipitation, subsurface water, and vegetation, the largest impacts were found for the moistest and coldest atmospheres. To find a suitable case study region, ERA5 data is plotted to find regions with a dry soil, and a moist and relatively cold atmosphere (table 3.2, Figure 4.9). It can be seen that most regions that light up in Figure 4.9 are relatively close to the coast and relatively mountainous, which can explain the high specific humidity and the low temperatures respectively. One of the most noticeable regions on the map is the Sinai peninsula, which will serve as a case study.

4.3.4 Summary

The two technology modes have different effects on the system: while the low evaporating technology has a larger positive effect on precipitation, subsurface water, and vegetation biomass, it causes significant warming of the surface. The high evaporating technology on the other hand can have a less strong, but positive effect if the atmosphere is cold and moist enough. The high evaporating technology also causes the temperature differences between day and night to reduce substantially, mostly by cooling the surface during the day, especially for the warmest atmospheres.

In short, the regions where the technology has the most potential of being effective have atmospheric profiles with high specific humidity and low atmospheric temperatures. These areas are mostly found near mountainous coasts. One such area is the Sinai peninsula which will be taken as a case study in the following section.

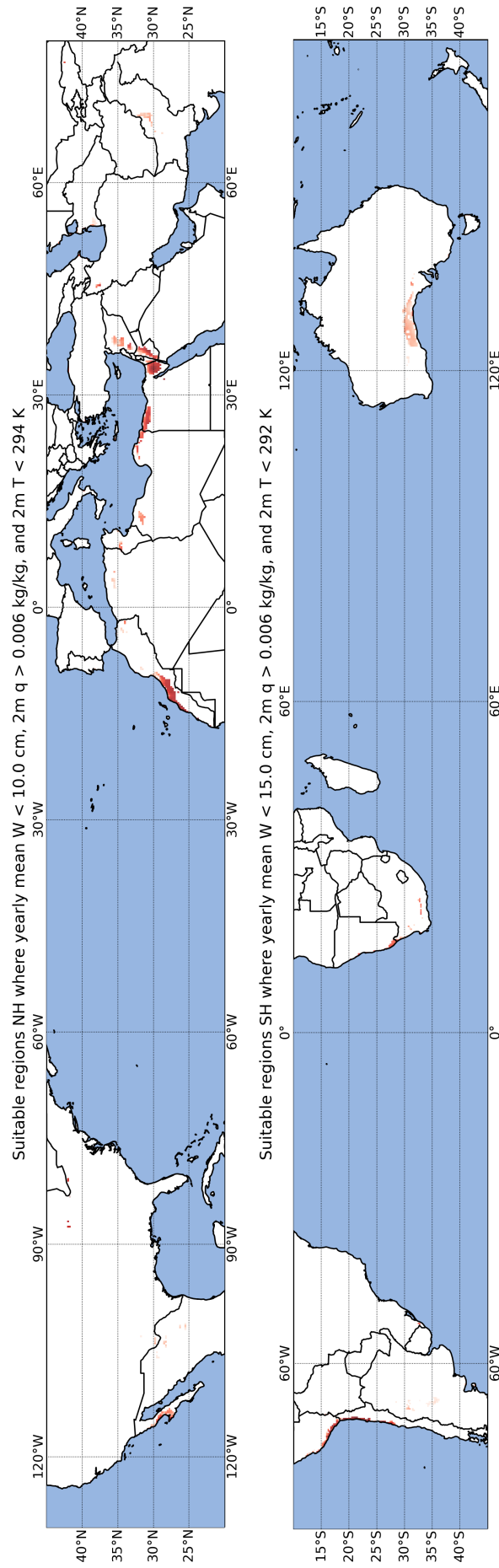


Figure 4.9: Red regions in the norther hemisphere (top) and the southern hemisphere (bottom) indicate the combination of a relatively dry soil, and a relatively moist and cold atmosphere.

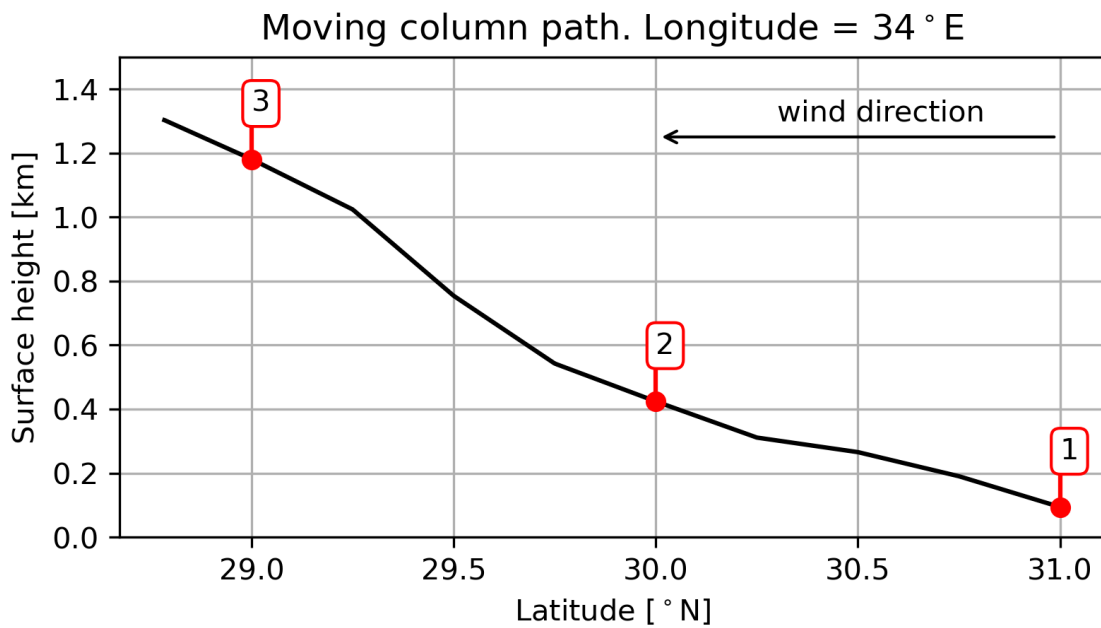
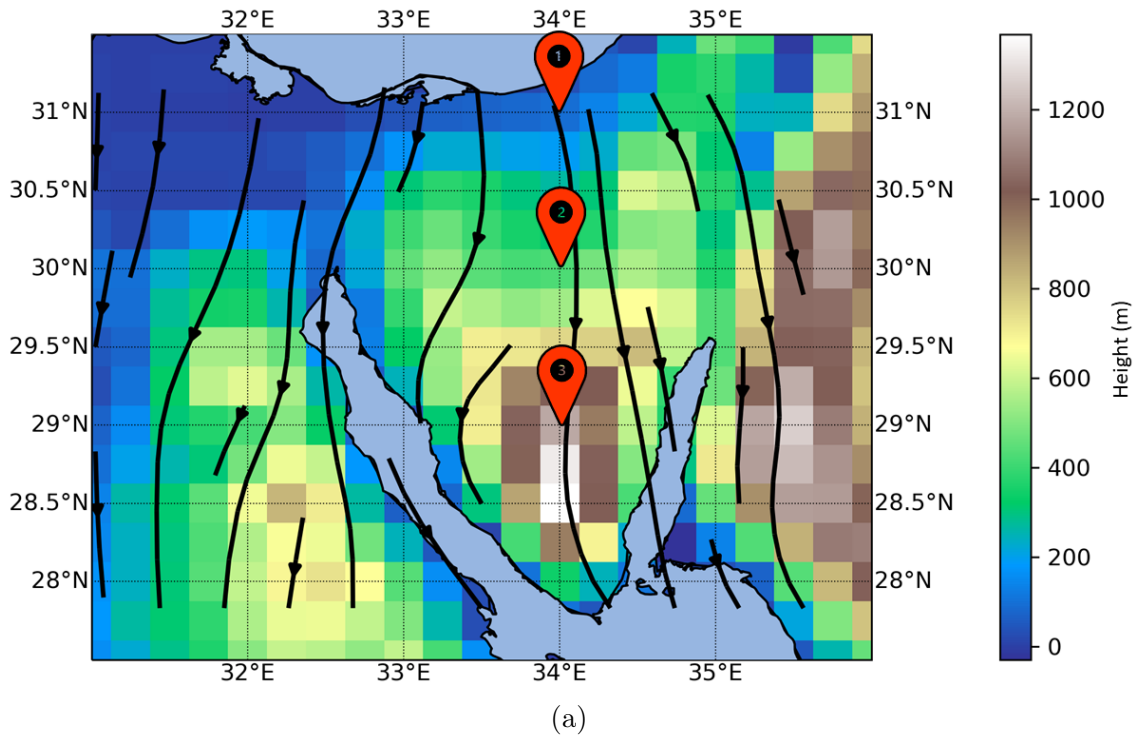


Figure 4.10: Surface height and wind direction from ERA5 geopotential and 10 m wind observations for October 2021 [13]. The three case study locations are indicated in red. (a) Map of the Sinai Peninsula, Egypt. (b) Cross-section of the surface height along the path of the atmospheric column up the mountain range of South Sinai for the moving column mode model runs.

4.4 Case study: Sinai peninsula

4.4.1 Introduction

The Sinai peninsula is part of Egypt, located in Asia. In the north, it borders the Mediterranean sea and in the south the Red Sea. Most of the Sinai peninsula has an aridity index < 0.05 which classifies this region as hyper-arid [7]. Moist air is transported from the Mediterranean sea southwards over the mountain range there, where the air cools down (Figure 4.10a). The month with the overall highest 2 m specific humidity is October, which is therefore the chosen month for this case study.

Three case study locations are chosen that have the same longitude of 34°E and different latitudes: 31°N , 30°N , and 29°N (Figures 4.10a and 4.10b). These locations lie on a streamline that approximately follows the 34th meridian east, which is followed for the MCM runs. The mean southward 10 m wind speed on this streamline between location 1 and 3 is 1.75 ms^{-1} , which is taken as the speed of the column for the runs in MCM.

4.4.2 Parameter tuning

Several model parameters were tuned to fit the model output to ERA5 monthly averaged reanalysis data for October 2021 (Table 3.3). The model has one day of run up time and then the model is tuned and plotted. The results of the parameter tuning for case study location 2 are shown and discussed here (Figures 4.11 and C.19). Case study locations 1 and 3 are shown in Figures C.16 - C.20.

The figures show that the incoming shortwave radiation of the model fits almost perfectly ($R^2 = 0.999$) to the reanalysis mean surface downward short-wave radiation flux (clear sky). No tuning was needed here. Furthermore, it was possible to obtain good fits for the net surface radiation and the surface (skin) temperature ($R^2 = 0.982$ and 0.951 respectively). The turbulent fluxes show a slight offset in timing of the increase and decrease, where the model shows an earlier peak in SHF ($R^2 = 0.897$) and a later peak in LHF ($R^2 = 0.752$) than the ERA5 reanalysis data. The model also overestimates the SHF during the night. The model slightly underestimates the 2m temperature ($R^2 = 0.663$) and shows more abrupt changes.

The boundary layer height (Figure 4.11) is shown as a reference but since the ERA5 reanalysis makes no distinction between CBLs and NBLs, no fit could be made. It can be clearly seen that the shape of the model ABL heights and ERA5 ABL height do not match: ERA5 heights show a decrease in height during the night instead of the growing NBL of the model. Furthermore, during the day the ERA5 heights show a concave shape which does not match the convex shape of early CBL growth from the model.

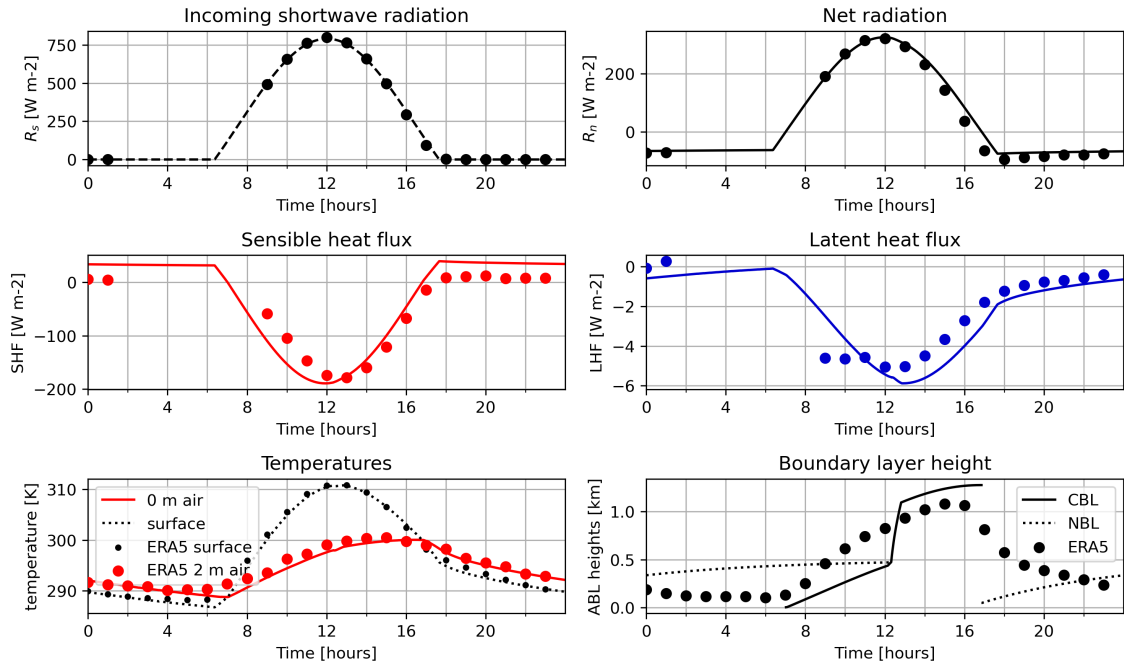


Figure 4.11: Model fit for for the Sinai peninsula case study location 2. Dots represent ERA5 monthly averaged reanalysis by hour of day for the month of October in the year 2021. The radiative fluxes have missing values for hours 2-8. Lines are the model run where the model parameters are tuned to fit the ERA5 energy fluxes and temperatures. R^2 values of the fits are for R_s : 0.999, R_n : 0.982, SHF : 0.897, LHF : 0.752, T_{2m} : 0.663, and T_s : 0.951. Boundary layer height is shown for comparison only, not for tuning.

4.4.3 Open model mode

Running the model in OM mode for the case study locations shows that the moisture flow in the system is mainly determined by advective fluxes (Table C.1). The largest inflow of subsurface water is the *orographic precipitation* and the largest outflow is drainage. In this case the high evaporating technology is the most effective because it increase the orographic precipitation, but no effect on local precipitation is found.

If the effect of advection is reduced by increasing Δx by a factor 10, it can be seen that advection still is the most determining factor in the system, but that the evaporating technology can have a positive, though very small, impact on precipitation: Precipitation goes from none to $0.003 \text{ mm day}^{-1}$ which is 0.17% of the daily evaporated seawater flux (Figure 4.12, Table C.2). The subsurface water shows a clear increase, both trough the reduced effect of natural evaporation and through the increase in orographic precipitation. This increase in subsurface water is not enough for vegetation growth.

4.4.4 Moving column mode

In MCM the air column is moved up the south Siani mountain range mountain with velocity in the y -direction $v = -1.75 \text{ m s}^{-1}$, following the path along the 34th meridian east as shown in Figure 4.10a and 4.10b. A run up time of the model is used of 9 hours, before the column starts to move. When the column moves, the

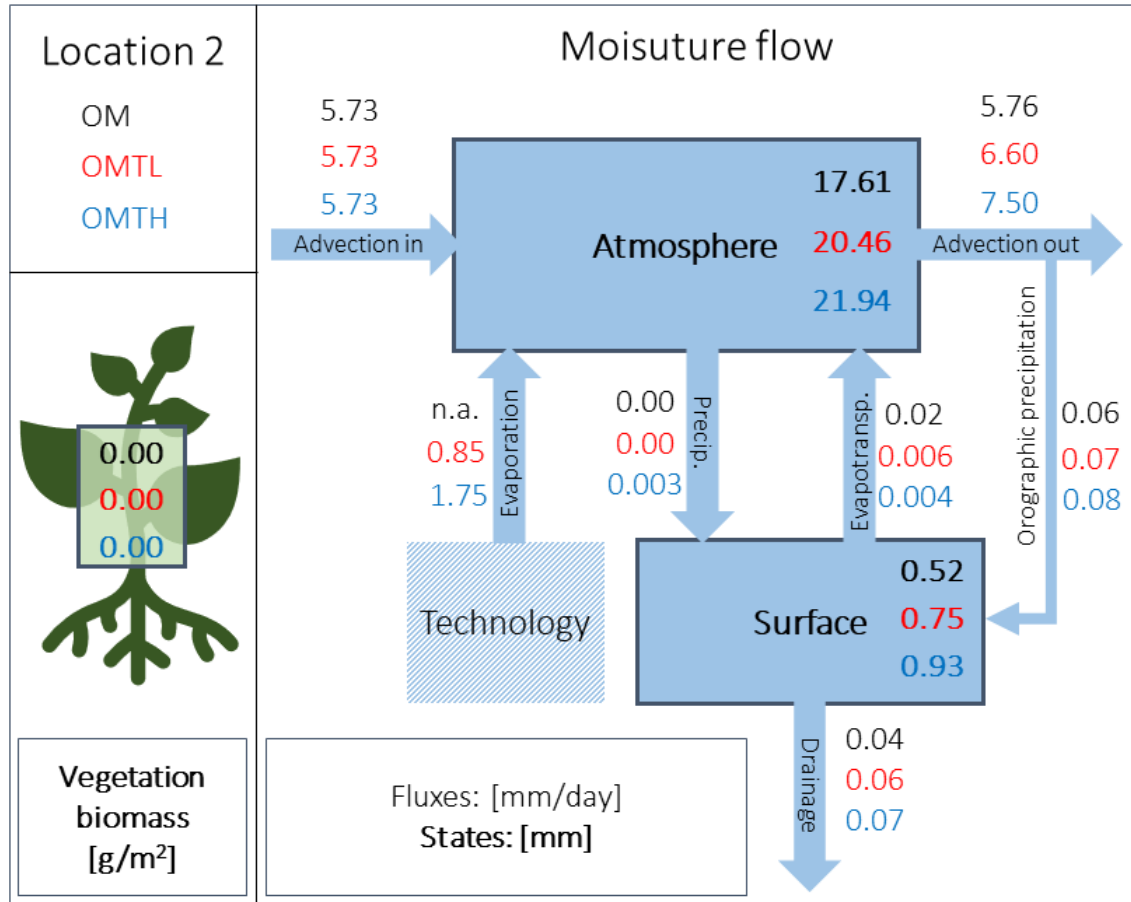


Figure 4.12: Water fluxes and water and biomass states in equilibrium for the Sinai peninsula case study location 2 for $\Delta x = 1000$ km. The model is run for three different model modes: Open model (OM, black), open model with low evaporating technology (OMTL, red), and open model with high evaporating technology (OMTH, blue). Monthly mean hourly ERA5 data on pressure levels is used for (potential) temperature, specific humidity, and wind speed boundary conditions.

first 10 km of the surface are assumed to be completely covered by the evaporation technology.

A comparison between results of a model run with technology (Figure 4.14) and without technology (Figure C.21) shows that the total increase in precipitation is 0.12 mm which all rains out on the third (last) model day, while the evaporation through technology takes place on the second model day. Comparing the amount of evaporated water through technology with the increase of rain shows that 30% of the evaporated water rains out.

4.4.5 Comparison with reanalysis data

ERA5 reanalysis data of the mean convective precipitation show that the highest mean convective precipitation rate over the Sinai is $0.104 \text{ mm day}^{-1}$ and is found on the highest point (Figure 4.13). In MCM without the technology on the model results show a precipitation rate of 1 mm day^{-1} on the third modelled day, where the highest point is not even reached. This shows that the model in MCM can regionally overestimate the amount of precipitation by at least a factor 10 compared to the

ERA5 reanalysis data. However, for the OM runs, no precipitation was found, which shows that the model in this mode can underestimate the amount of precipitation.

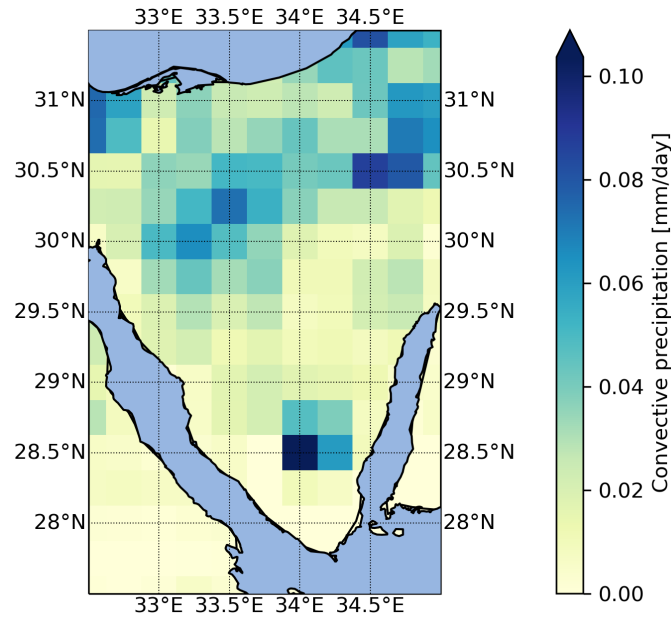


Figure 4.13: The Sinai Peninsula (Egypt) October 2021 daily mean convective precipitation rate (mm day^{-1}) from ERA5 monthly averaged data.

4.4.6 Summary

It was shown that the model can fit to ERA5 reanalysis data of radiation and turbulent fluxes at the surface and to surface and 2m temperature decently well. The modelled and ERA5 boundary layer heights do not match in shape. The case studies showed that the moisture flow in the system is mainly determined by advection, which makes the local effect of evaporation through technology small. However, the non-local impact can increase precipitation. In the model run in MCM it was found that 30% of the evaporated seawater rains out on the next day when going up the south Sinai mountain range. A comparison between the model results and ERA5 convective precipitation reanalysis data showed that the model in OM mode tends to underestimate convective precipitation, while the model in MCM tends to overestimate convective precipitation.

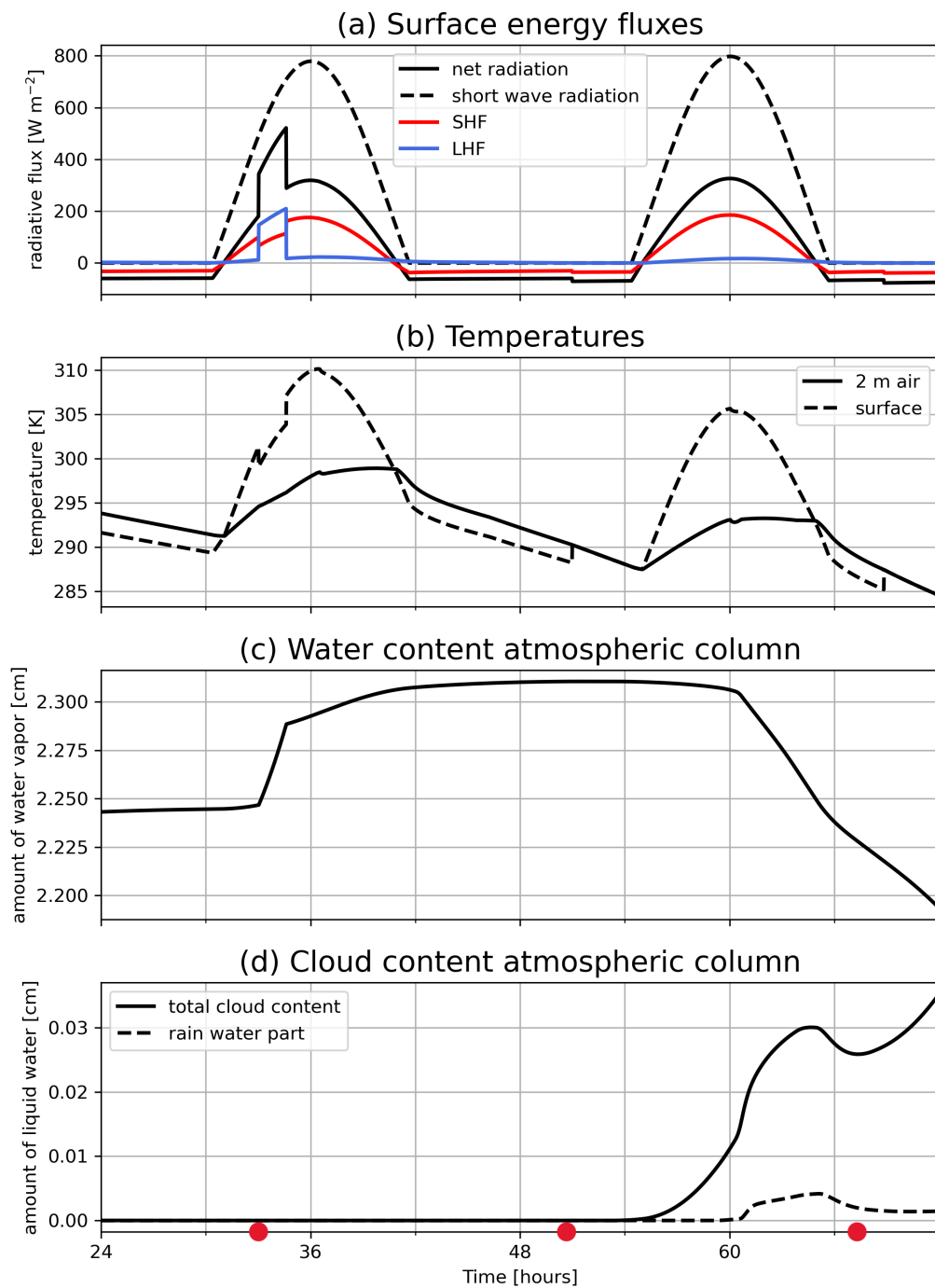


Figure 4.14: Time series of the run in moving column mode (MCM) where the first 33 hours are stationary after which the air column moves southward with a speed of 1.75 m s^{-1} . The first 10 km of land encountered by the column are totally covered by the evaporation technology. The case study locations passed (from 1 to 3, Figure 4.10b) are indicated with a red dot on the x-axis. The first 24 hours of the run are not shown. Panel a: Surface energy fluxes [W m^{-2}] with the incoming short-wave solar radiation (black, dashed), the net radiation (black, solid), the sensible heat flux (red), and the latent heat flux (blue). Panel b: Temperatures [K] of the surface (dashed) and near the surface (solid). Panel c: Water content [cm] of the atmospheric column up to 5 km high. Panel d: As panel c but for the cloud content (solid) and the rain water part of the cloud content (dashed). Continued on the next page.

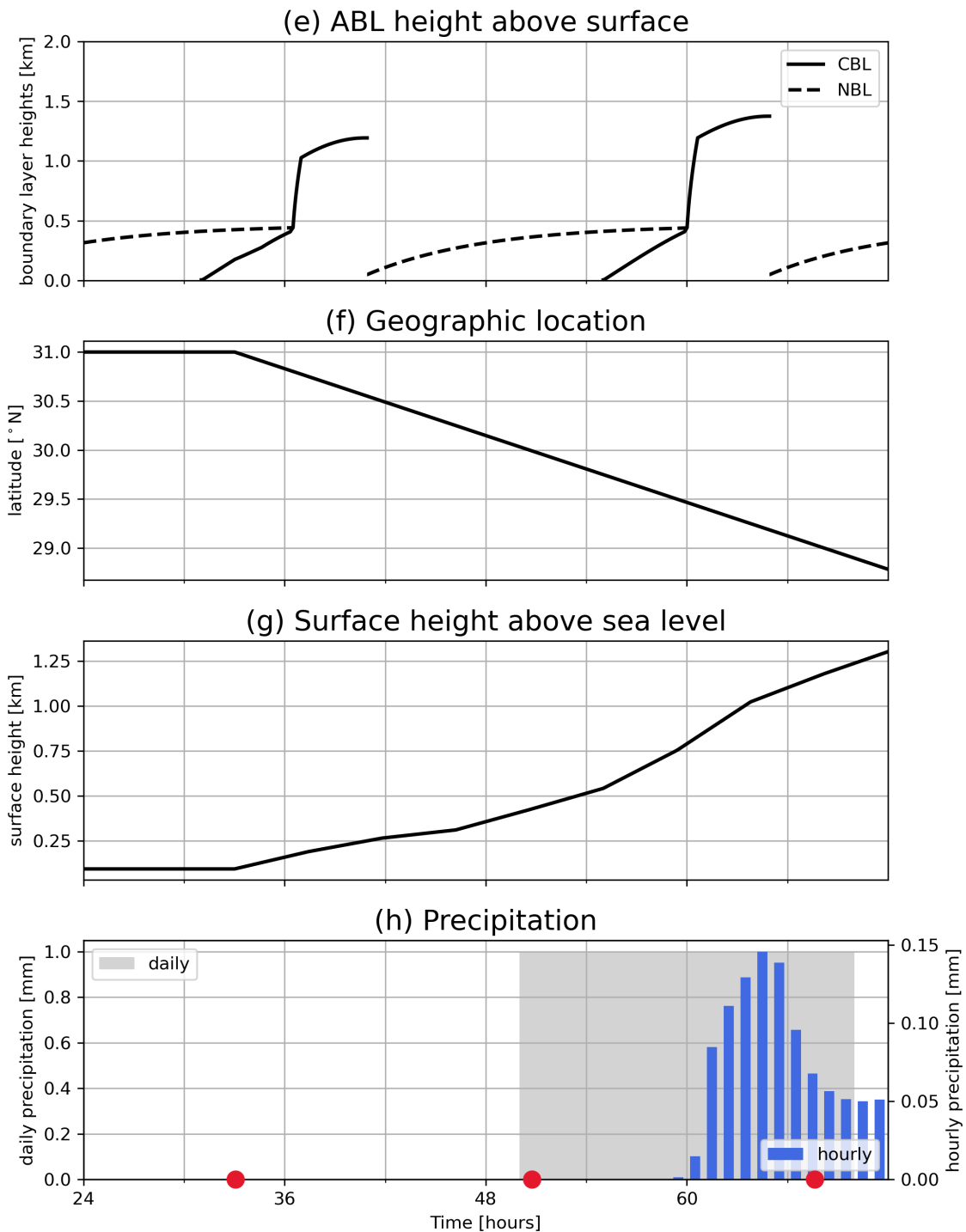


Figure 4.14: Continued from previous page. Panel e: Atmospheric boundary layer height [km] of the convective boundary layer (solid) and the nocturnal boundary layer (dashed). Panel f: Latitude of the geographic location [$^{\circ}$ N]. Panel g: Height of the surface above sea level [km]. Panel h: Daily (grey) and hourly (blue) precipitation [mm].

5 | Discussion

5.1 Introduction

The aim of this research project is to determine the potential of enhancing evaporation in arid and hyper-arid regions to restore the water cycle. To this end an atmospheric column model coupled to a surface model has been developed which has been used for sensitivity analysis and case studies. Although the setup of the model was relatively simple, the results were not always straightforward, which will be discussed first. Then, I will go back to discuss the model to determine where the simplicity is a feat, and where it may have led to problems, i.e. which priorities are there for model improvements. Then the used data and the technology itself are discussed and a general outlook is given.

5.2 The results

The closed model runs show the counter-intuitive results where more initial atmospheric moisture leads to less vegetation biomass in equilibrium. This is likely caused by the constrained put on the subsurface water by Equations 2.25 and 2.26. I was not able to provide a clear causal explanation for this behaviour, but I can say that this behaviour is most likely an artifact of the model and does not represent a real life situation. The CM mode runs to equilibrium should therefore not be used for projections.

The results in the OM and OMT modes show that the energy partitioning between sensible and latent heat fluxes at the surface determines the occurrence of convective precipitation. The technology can be effective by affecting the energy partitioning in the right way, which depends on the atmospheric conditions, as was expected from previous studies [21].

As a first example, locations with a high atmospheric moisture content mostly depend on the development of a high CBL for the occurrence of convective precipitation. In this case, to enhance precipitation, the technology should not inhibit the *SHF* and therefore should not evaporate too much. The finding that enhanced evaporation through technology can be repressive for rainfall when it suppresses the growth of the convective boundary layer is in line with findings from Seneviratne et al. [32].

As a second example, locations with low atmospheric temperatures do depend on the availability of atmospheric moisture for the occurrence of precipitation. Therefore, to enhance precipitation here, the technology can evaporate more. However, a high evaporating technology may yield better results when used for non-local precipitation enhancement as is shown by the case studies in moving column mode.

Although tuning of the model to the case study locations yielded decent fits for the surface radiative and turbulent fluxes, the model tended to over or underestimate the amount of precipitation, depending on the model mode.

Lastly, it was found that it was not possible to increase vegetation biomass in the case study regions through the use of the technology. Locally, this could be due to the large effect of advection on the model, which weakened the effect of the enhanced evaporation. It should be noted that the model fit and runs were performed for the month of October only, since this month had the most promising atmospheric conditions for the technology to be effective. However, October does not have optimal conditions for CBL growth because of less incoming solar radiation than in summer months. It would be interesting to investigate the effect of the technology in summer and determine if, even though atmospheric conditions are less favorable, the evaporation technology could be more effective because of the increase in net radiation at the surface.

5.3 The model

In this research project, a coupled one column atmospheric boundary layer - surface model was developed with the aim of exploring the potential of evaporation technology to restore the water cycle in arid regions. The starting point of this model is the often used boundary layer slab model [e.g. 9, 20, 21, 27]). This model is expanded by a *night regime*, which enables the modelling of a diurnal cycle and consecutive days without having to re-initialize the model every morning. Furthermore, in this project a step is taken to improve the physics of precipitation by including the development of clouds, where this was neglected in other models [20, 21]. An interesting result of these model developments is the possibility of mist formation at night. Although not explicitly shown in the results, mist was included in the total cloud content.

Using a relatively simple model has its benefits and caveats. Benefits are that constraining oneself to only modelling the most important processes makes that the the model results can be explained from the modelled assumptions. Furthermore, it is a quick and cost effective way of gaining insights in a complex system. Caveats of the simplicity are that the model cannot capture all dynamics and processes which may lead to over and underestimations or even misrepresentations of certain dynamics. Therefore, results should be interpreted with care.

An uncertainty from the slab model is the convective boundary layer height. Equation 2.14 explains 80-90% of CBL growth [35]. However, using Equation 3.1 to determine $\overline{(\theta'\omega')_h}$ makes the CBL growth less accurate. For the sensitivity analysis, CBLs are found to grow beyond the common maximum CBL height of 2 km, which is possible for desert regions that have a large *SHF*. However, the slab model may not be suited for these high CBLs. This is because the assumption of constant air density in the whole column may lead to significant over-estimations of air density and under-estimations of pressure and temperature higher up in the atmospheric column (Figure C.22), which could lead to over-estimations in cloud formation and precipitation.

Another caveat of the model is that the atmospheric radiation and the ground heat flux are parameterized. This causes an imbalance of radiation in the system. In the closed model mode, this leads to unrealistic heating of the atmosphere and

surface. However, this problem can be solved by relaxing the atmospheric temperatures to a boundary atmospheric profile through the addition of an advection term as is done for the CM2 mode.

For completely dry atmospheres, the used parameterization for incoming long-wave radiation at the surface causes problems. Since this parameterization depends on the vapor pressure, which is zero in these cases, there is no back radiation, which causes the net radiation at the surface to be very small which also causes the *SHF* to become very small. With the modelled switches between the day and the night regimes, this leads to very long nights and thus prolonged periods of cooling. Furthermore, the CBL during the day does not grow higher than 200 m which prevents the ABL from entraining warm air from the free atmosphere. To resolve this problem, a different parameterization for back radiation could be used.

Since cloud dynamics and rainfall are complex processes, this research limits the modelling of cloud processes to stratocumulus clouds where the assumption is made that the clouds are part of the convective mixed layer [35]. This is a step forward in the modelling of precipitation if compared to other studies using a CBL slab model such as Konings et al. [20] and Konings, Katul, and Porporato [21]. A downside of this approach was the possible occurrence of instabilities in the atmospheric column through local heating and cooling because of condensation and evaporation.

Stratum et al. [34] show a different approach where cumulus clouds are assumed to grow on top of the boundary layer and interact with the boundary layer through a mass flux into the cloud layer. This approach allows for several negative feedbacks between the development of clouds and the growth of the convective boundary layer, which could not be accounted for in the current approach. However, Stratum et al. [34] limit their modelling to the subcloud layer and treat the existence of clouds as a boundary condition. To expand the current model with the methods by Stratum et al. [34] would ask for an expansion of their model to include the cloud layer. Furthermore, radiative effects of clouds could be considered.

Lastly, model runs in open model mode showed that the equilibrium results were insensitive to initial conditions, which means that a restoration of the water cycle could not be modelled. In other words, the technology had to be included continuously to show any effect of this technology. This might be because of the dominant impact of advection on the water fluxes in equilibrium, but this has to be researched further.

5.4 The data

Because of a lack of direct observations on the Sinai peninsula, ERA5 reanalysis data was used to tune the model to the case study regions. This brings some uncertainties because the ERA5 reanalysis is model based and can be less accurate for regions with little observations. The Sinai peninsula is even within the region where ERA5 precipitation data show the largest inconsistencies with satellite observations [3]. Furthermore, several data points were missing for the radiative and turbulent fluxes at the surface. The boundary layer height from the reanalysis showed quite different behaviour than the modelled boundary layers. Guo et al. [10] found that ERA5 had the best boundary layer height when compared to other reanalysis products and radiosonde determined boundary layers. They found an underestimation of the

height by around 130 m for CBLs, which support the CBL height results of the model used in this research.

5.5 The technology

From the sensitivity analysis it is found that the technology has the most potential for increasing precipitation and subsurface water in regions with a cold and moist atmosphere, but results vary for technologies with different energy partitioning, i.e. technologies with high evaporation, low evaporation, or even no evaporation. For moist and warm atmospheres, the high evaporating technology (OMTH) can have a negative impact on the amount of precipitation.

For the low evaporating technology (OMTL), a trend was visible where the larger the amount of precipitation without the technology, the larger the amount of precipitation *increase* with the technology. This indicates that the potential of the technology to restore water cycles may be larger for semi-arid areas than for hyper-arid or arid areas, but this should be researched further. Furthermore, the no-evaporation technology, i.e. partially covering the surface with a dark cloth, should be further investigated as a way to potentially increase precipitation in regions with a moist atmosphere, because the results showed that this might be more effective than a technology that does evaporate water.

It is important to note that the effects of the technology are not limited to precipitation enhancement or inhibition and are not contained locally. As the results showed, the low evaporating technology could have a local warming effect. The high evaporating technology on the other hand can cause extreme surface cooling for regions with high atmospheric temperatures. While not the purpose of the technology, it could be beneficial in certain locations.

5.6 General outlook

In the previous sections, I made some recommendations for further research regarding model improvements and the technology. Here I will give a more general outlook. This research has shown the importance of considering the effect regreening initiatives on the energy partitioning at the surface. This can be related to soil properties regarding water retention, vegetation types, and the drought reaction of specific vegetation types. Branch and Wulfmeyer [5] found that convective rainfall can be enhanced over a desert *Jajoba chinensis* plantation on dry days when stomatal closure decreases the latent heat flux and increases the sensible heat flux. A parallel can be drawn between these vegetation properties and the low evaporating technology. This research therefore stresses the importance of not only understanding the energy partitioning processes of the technology, but also of the vegetation when designing water cycle restoration projects.

Lastly, I would like to remark that there is a general concern that regreening projects can harm local communities and biodiversity [31]. To prevent this, research is needed into the broader environmental and social impacts of the projects. In this exploratory research I attempted to find the conditions and regions where the evaporation technology can be effective. However, it may be better to reverse the question, e.g. if there is a degraded area where the community and biodiversity

would benefit from greening, could the technology be helpful in this location, and what type of technology would be needed? This reversed train of thought would improve the chances of putting the needs of the local communities first.

6 | Conclusion

With this research I have tried to find an answer to the question: Can evaporation through technology potentially be used for water cycle restoration in arid and hyper-arid regions? To this end, I developed a simple coupled atmosphere-surface model which extended the use of the convective boundary layer slab model by including cloud formation and precipitation and including the formation of a nocturnal boundary layer to allow the modelling of a diurnal cycle.

It was found that convective precipitation is a trade off between convective boundary layer height and boundary layer humidity, which are mainly determined by surface fluxes and advection. With a seawater evaporating technology it is possible to increase the amount of energy at the surface by lowering the albedo and through those means, to both support a high convective boundary layer and increase the humidity, therefore supporting the formation of clouds and precipitation.

The effectiveness of the technology is mostly determined by the atmospheric specific humidity and temperature. The local atmosphere also determines which type of technology should be used: high evaporating or low evaporating technology. In general, the technology has the potential to be effective in regions with a relatively moist and cold atmosphere. These regions are mainly found near coast and/or in highly elevated areas.

For the Sinai peninsula it was not found that the technology could restore the water cycle. However, it may be possible to increase the amount of precipitation, if the technology is placed in such a way that the extra moisture is advected up the mountain range of South Sinai.

This research can not provide a definite answer to the research question because the model was not sensitive to initial conditions. However, there are clear indications that when considering the effects of the changes in energy partitioning at the surface, it may be possible to enhance convective precipitation using the technology in certain arid and hyper-arid regions that have an atmosphere that is moist and cold enough. This research has shown the importance of considering the atmospheric effects of energy partitioning at the surface when planning water cycle restoration projects.

Acknowledgements

I want to express my thanks to everyone who supported me during this research. First of all, I am very grateful for my daily supervisor Jolanda Theeuwes for taking the time to discuss my progress and the problems I encountered weekly and for giving me useful insights to help me along. I also would like to extend my sincere thanks to my additional advisor Bert Hamelers for giving me the opportunity to present the monthly developments of my research. These meetings helped me tremendously in keeping me focused on the main issue and not get lost in details. I would like to thank my IMAU supervisor and first corrector Aarnout van Delden for his enthusiasm and for lending me his expertise in atmospheric modelling. I am also thankful for my second corrector Michiel Baatsen for taking the time to evaluate this thesis. Furthermore, I want to express many thanks to the Copernicus Institute and Stefan Dekker in particular, and to the Weather Makers for their interest and engagement with this research. Moreover I am grateful for all my class mates who I spend a lot of time with on the sixth floor of the Buys-Ballot Building. It wouldn't have been half as fun to do this research without having all the lunches and coffee breaks together. Lastly, I would like to thank my friends, family, and in particular Sjoerd for their support and for making sure I also engaged in recreational activities outside of this research.

Bibliography

- [1] 2022. URL: <https://phdpositionswetsus.eu/phd-project-3/>.
- [2] Ahmed Alkaisi, Ruth Mossad, and Ahmad Sharifian-Barforoush. “A review of the water desalination systems integrated with renewable energy”. In: *Energy Procedia* 110 (2017), pp. 268–274.
- [3] Alireza Arabzadeh et al. “Global intercomparison of atmospheric rivers precipitation in remote sensing and reanalysis products”. In: *Journal of Geophysical Research: Atmospheres* 125.21 (2020), e2020JD033021.
- [4] Sara Bonetti et al. “The influence of water table depth and the free atmospheric state on convective rainfall predisposition”. In: *Water Resources Research* 51.4 (2015), pp. 2283–2297.
- [5] Oliver Branch and Volker Wulfmeyer. “Deliberate enhancement of rainfall using desert plantations”. In: *Proceedings of the National Academy of Sciences* 116.38 (2019), pp. 18841–18847.
- [6] Wilfried Brutsaert. “On a derivable formula for long-wave radiation from clear skies”. In: *Water resources research* 11.5 (1975), pp. 742–744.
- [7] M. Cherlet et al. *World Atlas of Desertification*. 3rd ed. Publication Office of the European Union, 2018. ISBN: 978-92-79-75349-7. DOI: 10.2760/06292.
- [8] Aarnout van Delden. *Atmospheric Dynamics Chapter 1 Introduction to the Atmosphere*. <https://webpace.science.uu.nl/~delde102/AtmosphericDynamics.htm>. 2021.
- [9] Livia S Freire and Nelson L Dias. “Residual layer effects on the modeling of convective boundary layer growth rates with a slab model using FIFE data”. In: *Journal of Geophysical Research: Atmospheres* 118.23 (2013), pp. 12–869.
- [10] Jianping Guo et al. “Investigation of near-global daytime boundary layer height using high-resolution radiosondes: first results and comparison with ERA5, MERRA-2, JRA-55, and NCEP-2 reanalyses”. In: *Atmospheric Chemistry and Physics* 21.22 (2021), pp. 17079–17097.
- [11] Chiel C van Heerwaarden. *Surface evaporation and water vapor transport in the convective boundary layer*. 2011.
- [12] H Hersbach et al. “ERA5 monthly averaged data on pressure levels from 1979 to present. Copernicus Climate Change Service (C3S) Climate Data Store (CDS)”. In: *Copernicus Climate Change Service (C3S) Climate Data Store (CDS)* (2019).

- [13] H Hersbach et al. “ERA5 monthly averaged data on single levels from 1979 to present.” In: *Copernicus Climate Change Service (C3S) Climate Data Store (CDS)* (2019).
- [14] Robert A Houze Jr. “Orographic effects on precipitating clouds”. In: *Reviews of Geophysics* 50.1 (2012).
- [15] Moses G Iziomon, Helmut Mayer, and Andreas Matzarakis. “Downward atmospheric longwave irradiance under clear and cloudy skies: Measurement and parameterization”. In: *Journal of Atmospheric and Solar-Terrestrial Physics* 65.10 (2003), pp. 1107–1116.
- [16] Jehn-Yih Juang et al. “Hydrologic and atmospheric controls on initiation of convective precipitation events”. In: *Water Resources Research* 43.3 (2007).
- [17] Justdiggitt. *What we do*. Dec. 2021. URL: <https://justdiggitt.org/what-we-do/>.
- [18] Edwin Kessler. “On the distribution and continuity of water substance in atmospheric circulations”. In: *On the distribution and continuity of water substance in atmospheric circulations*. Springer, 1969, pp. 1–84.
- [19] CP Kim and D Entekhabi. “Feedbacks in the land-surface and mixed-layer energy budgets”. In: *Boundary-Layer Meteorology* 88.1 (1998), pp. 1–21.
- [20] Alexandra G Konings et al. “Drought sensitivity of patterned vegetation determined by rainfall-land surface feedbacks”. In: *Journal of Geophysical Research: Biogeosciences* 116.G4 (2011).
- [21] Alexandra G. Konings, Gabriel G. Katul, and Amilcare Porporato. “The rainfall-no rainfall transition in a coupled land-convective atmosphere system”. In: *Geophysical Research Letters* 37 (14 July 2010). ISSN: 00948276. DOI: 10.1029/2010GL043967.
- [22] John L Monteith. “Evaporation and environment”. In: *Symposia of the society for experimental biology*. Vol. 19. Cambridge University Press (CUP) Cambridge. 1965, pp. 205–234.
- [23] United Nations. *The United Nations Decade on Ecosystem Restoration Strategy*. 2021. URL: <https://wedocs.unep.org/bitstream/handle/20.500.11822/31813/ERDStrat.pdf?sequence=1&isAllowed=y>.
- [24] Sandip Pal et al. “When and where horizontal advection is critical to alter atmospheric boundary layer dynamics over land: The need for a conceptual framework”. In: *Atmospheric Research* 264 (2021), p. 105825.
- [25] Amilcare Porporato. “Atmospheric boundary-layer dynamics with constant Bowen ratio”. In: *Boundary-Layer Meteorology* 132 (2 2009), pp. 227–240. ISSN: 00068314. DOI: 10.1007/s10546-009-9400-8.
- [26] Hans R Pruppacher and James D Klett. “Microstructure of atmospheric clouds and precipitation”. In: *Microphysics of clouds and precipitation*. Springer, 2010, pp. 10–73.
- [27] Camilo Rey-Sanchez et al. “Evaluation of Atmospheric Boundary Layer Height From Wind Profiling Radar and Slab Models and Its Responses to Seasonality of Land Cover, Subsidence, and Advection”. In: *Journal of Geophysical Research: Atmospheres* 126.7 (2021), e2020JD033775.

- [28] Gerard H. Roe, David R. Montgomery, and Bernard Hallet. “Orographic precipitation and the relief of mountain ranges”. In: *Journal of Geophysical Research: Solid Earth* 108 (B6 June 2003). ISSN: 2169-9356. DOI: 10.1029/2001jb001521.
- [29] B Schaeffli et al. “An analytical model for soil-atmosphere feedback”. In: *Hydrology and Earth System Sciences* 16.7 (2012), pp. 1863–1878.
- [30] Christoph Schär et al. “The soil–precipitation feedback: A process study with a regional climate model”. In: *Journal of Climate* 12.3 (1999), pp. 722–741.
- [31] Nathalie Seddon. “Harnessing the potential of nature-based solutions for mitigating and adapting to climate change”. In: *Science* 376.6600 (2022), pp. 1410–1416.
- [32] Sonia I Seneviratne et al. “Investigating soil moisture–climate interactions in a changing climate: A review”. In: *Earth-Science Reviews* 99.3-4 (2010), pp. 125–161.
- [33] Mohamed S Smeda. “A bulk model for the atmospheric planetary boundary layer”. In: *Boundary-Layer Meteorology* 17.4 (1979), pp. 411–427.
- [34] Bart JH van Stratum et al. “Subcloud-layer feedbacks driven by the mass flux of shallow cumulus convection over land”. In: *Journal of the Atmospheric Sciences* 71.3 (2014), pp. 881–895.
- [35] Roland B Stull. *An introduction to boundary layer meteorology*. Vol. 13. Springer Science & Business Media, 1988.
- [36] *The Great Green Wall*. URL: <https://www.greatgreenwall.org/about-great-green-wall>.
- [37] Xin-ping Wang et al. “Probabilistic model predicts dynamics of vegetation biomass in a desert ecosystem in NW China”. In: *Proceedings of the National Academy of Sciences* 114.25 (2017), E4944–E4950.
- [38] Sofie A te Wierik et al. “Reviewing the Impact of Land Use and Land-Use Change on Moisture Recycling and Precipitation Patterns”. In: *Water Resources Research* 57.7 (2021), e2020WR029234.
- [39] Liang Zhu et al. “Evolutionary trend of water cycle in Beichuan River Basin of China under the influence of vegetation restoration”. In: *Journal of Groundwater Science and Engineering* 9.3 (2021), pp. 202–211.

A | Table of used symbols

Overview of all variables, parameters, and constants and their units used in the model. Values are given for the parameters and constants which are used in all model runs unless stated otherwise in the methods (Chapter 3). If applicable, the source of the parameter values is given in brackets.

Variables

α	-	surface albedo
δ_s	rad	solar declination
$\Delta\theta_s$	K m	accumulated cooling of the NBL
$H_{\Delta\theta}$		
Δ	Pa °C ⁻¹	slope of the Clausius-Clapeyron equation
ψ	-	precipitation to evaporation ratio
θ	K	potential temperature
θ_m	K	mean potential temperature of the NBL
θ_s	K	potential temperature of the surface
B	kg m ⁻²	vegetation biomass
C	m s ⁻¹	condensation rate
e	kg kg ⁻¹	water vapor pressure
E_{ET}	m s ⁻¹	technology evaporation rate
e_{sat}	kg kg ⁻¹	saturation vapor pressure
E_c	m s ⁻¹	cloud evaporation rate
E_s	m s ⁻¹	soil evaporation rate
E_t	m s ⁻¹	vegetation transpiration rate
G	W m ⁻²	ground heat flux
g^{Es}	m s ⁻¹	surface conductance
g^{Et}	m s ⁻¹	stomatal conductance
h	m	boundary layer height or thickness
LHF	W m ⁻²	latent heat flux
p	Pa	atmospheric pressure
P	m s ⁻¹	precipitation rate
q	kg kg ⁻¹	specific humidity
$Q_{evap,cond}$	K s ⁻¹	sensible heat produced or consumed by condensation or evaporation
q_{sat}	kg kg ⁻¹	saturation specific humidity
q_L	kg kg ⁻¹	cloud content
q_R	kg kg ⁻¹	atmospheric rain water content

Q_R	K m s^{-1}	radiative cooling acting on the NBL
Q_T	K m s^{-1}	total heat flux acting on the NBL
R_n	W m^{-2}	net radiation at the surface
R_s	W m^{-2}	incoming solar radiation
r_s	s m^{-1}	surface resistance
r_{sat}	kg kg^{-1}	saturation mixing ratio
SHF	W m^{-2}	sensible heat flux
T_{air}	K	atmospheric temperature
T_r	-	net sky transmissivity
T_s	K	temperature of the surface
W	m	subsurface water
w_e	m s^{-1}	entrainment velocity
$(\theta'\omega')_s$	K m s^{-1}	sensible heat mass flux
$(q'\omega')_s$	$\text{kg kg}^{-1} \text{ m s}^{-1}$	latent heat mass flux

Parameters

α_{ET}	0.1	evaporation technology albedo
α_{max}	0.4	maximum albedo, corresponding to an un-vegetated state
α_{min}	0.1	minimum albedo, corresponding to a fully vegetated state
α_1	$10 \text{ m}^2 \text{ kg}^{-1}$ [20]	amount of leaf area per unit biomass
Δx	100000 m	assumed horizontal extend of the model when advection is included
ε_a	10^{-5} s^{-1}	atmospheric emissivity
ε_s	1	surface emissivity
γ_θ	5 K km^{-1}	slope of the linear free atmospheric potential temperature
γ_q	$0 \text{ kg kg}^{-1} \text{ m}^{-1}$	slope of the linear free atmospheric specific humidity
ϕ	35°N	latitude
ϕ_θ	300 K	intersect of the linear free atmospheric potential temperature
ϕ_q	$6 \cdot 10^{-3} \text{ kg kg}^{-1}$	intersect of the linear free atmospheric specific humidity
Φ_r	0.409 rad [11]	tilt of the earth's axis relative to the elliptic
ρ_{air}	1.1 kg m^{-3}	density of air
σ_A	0	fraction of sky covered by active clouds
τ	13.5 hours	NBL scaling time
a_1	10^{-5} s^{-1} [33]	proportionality constant radiative cooling
a_2	$0.5 \cdot 10^{-3} \text{ kg m}^{-3}$ [18]	cloud conversion threshold
A_R	0.2 [19, 25]	ratio of the sensible heat flux at the top of the ABL to the surface sensible heat flux
b	0.0196 day^{-1} [37]	max. assimilation rate ¹

APPENDIX A. TABLE OF USED SYMBOLS

B_{max}	1 kg m ⁻²	max. vegetation biomass D
109	day of the year	
d_1	0.0071 day ⁻¹ [37]	death rate ¹
f_{return}	0.01	fraction of the atmospheric water leaving the column through advection that returns to the system as subsurface water
g^{ET}	0.01 m s ⁻¹	evaporation technology surface conductance
g_{max}^{Es}	0.0005 m s ⁻¹	maximum surface conductance
g_{max}^{Et}	0.001 m s ⁻¹	maximum stomatal conductance
k_1	10 ⁻⁴ s ⁻¹	condensation rate
k_2	10 ⁻⁴ s ⁻¹	evaporation rate
k_3	10 ⁻³ s ⁻¹ [18]	cloud autoconversion coefficient
k_4	2.5 · 10 ⁻³ kg m ⁻² [20]	saturation constant for the evaporation reduction function due to shade from biomass, ignoring biomass morphology.
n	1	determines shape of the temperature profile of the NBL. $n = 1$ implies a linear profile [35].
p_0	101300 Pa	reference pressure
p_s	101300 Pa	surface pressure
r_a	50 s m ⁻¹ [11]	atmospheric resistance
r_P	10 ⁻³ s ⁻¹	precipitation fall rate
r_w	0.08 d ⁻¹ [20]	drainage rate
U_{day}	1 m s ⁻¹	wind speed during the day
U_{night}	0.1 m s ⁻¹	wind speed during the night
W^*	1.93 · 10 ⁻² m [37]	incipient stomatal closure
W_{wilt}	3.9 · 10 ⁻³ m [37]	wilting point

Constants

ϵ	0.622	R_d/R_v
γ	66.75 Pa °C ⁻¹	psychrometric constant
λ	2.45 · 10 ⁶ J kg ⁻¹	latent heat of vaporization of water
ρ_{H_2O}	1.0 · 10 ³ kg m ⁻³	density of water
σ	5.67 · 10 ⁻⁸ W m ⁻² K ⁻⁴	Stefan-Boltzmann constant
c_p	1004 J kg ⁻¹ K ⁻¹	specific heat of air at constant pressure
c_v	717 J kg ⁻¹ K ⁻¹	specific heat of air at constant volume
g	9.81 m s ⁻²	gravitational acceleration
k_v	0.4	von Kármán's constant
R_d	287 J kg ⁻¹ K ⁻¹	specific gas constant for dry air
R_v	461.5 J kg ⁻¹ K ⁻¹	specific gas constant for water vapor
W_0	1353 W m ⁻²	solar irradiance (solar constant)

¹In model runs to equilibrium the value is multiplied by 100 to ensure a faster reach of the equilibrium which does not affect the equilibrium itself.

B | Appendix to methods

B.1 Additional formulas

B.1.1 Solar radiation

Following Heerwaarden [11], the incoming shortwave radiation from the sun is

$$R_s(t) = W_0 T_r \sin(\Psi) \quad (\text{B.1})$$

where W_0 is the solar constant, T_r the net sky transmissivity, that takes into account the influence of radiative path length and atmospheric absorption and scattering using:

$$T_r = 0.6 + 0.2 \sin(\Psi) \quad (\text{B.2})$$

Through Ψ , R_s depends on the latitude, day of the year, and the time of the day according to

$$\sin(\Psi) = \sin(\phi) \sin(\delta_s) - \cos(\phi) \cos(\delta_s) \cos\left(2\pi \frac{t}{24}\right) \quad (\text{B.3})$$

where t is the time and ϕ the latitude (positive north of the Equator). δ_s is the solar declination, which is a function of the day of the year:

$$\delta_s = \Phi_r \cos\left(2\pi \frac{D - 176}{365}\right) \quad (\text{B.4})$$

where D is the day of the year and Φ_r is tilt of the earth's axis relative to the elliptic.

B.1.2 Temperature, pressure, and density

The air temperature at a certain pressure level (p) can be found from the potential temperature with

$$\theta = T_{air} \left(\frac{p_s}{p}\right)^{\frac{R_d}{c_p}} \quad (\text{B.5})$$

where p_s is the reference pressure at the surface and $R_d = c_p - c_v$ is the specific gas constant for dry air [8]. c_p and c_v are the specific heat capacities at constant pressure and constant volume respectively. The pressure at a certain height can be found using the hydrostatic balance

$$\frac{\partial p}{\partial z} = -\rho_{air} g \quad (\text{B.6})$$

where ρ_{air} is the density of air, which can be found using the equation of state

$$p = R_d \rho_{air} T_{air} \quad (\text{B.7})$$

B.2 Overview of data used

Variable	Units
ERA 5 monthly averaged data on single levels, reanalysis by hour of day [13]	
Surface pressure	Pa
2m temperature	K
Skin temperature	K
10m u-component of wind	ms-1
10m v-component of wind	ms-1
Volumetric soil water layer 1	m ³ m ⁻³
Volumetric soil water layer 2	m ³ m ⁻³
Volumetric soil water layer 3	m ³ m ⁻³
Leaf area index, high vegetation	m ² m ⁻²
Leaf area index, low vegetation	m ² m ⁻²
Forecast albedo	Dimensionless
Mean surface downward short-wave radiation flux, clear sky	W m ⁻²
Mean surface net short-wave radiation flux, clear sky	W m ⁻²
Mean surface net long-wave radiation flux, clear sky	W m ⁻²
Mean surface sensible heat flux	W m ⁻²
Mean surface latent heat flux	W m ⁻²
Boundary layer height	m
Mean convective precipitation rate	kg m ⁻² s ⁻¹
Mean total precipitation rate	kg m ⁻² s ⁻¹
Geopotential	m ² s ⁻²
ERA5 monthly averaged data on pressure levels, reanalysis by hour of day [12]	
Temperature	K
Specific humidity	kg kg ⁻¹
U-component of wind	m s ⁻¹
V-component of wind	m s ⁻¹

C | Appendix to results

C.1 CM sensitivity

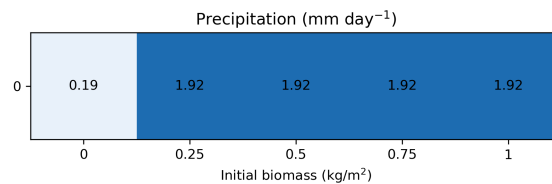


Figure C.1: Precipitation sensitivity in CM1 mode to initial biomass.

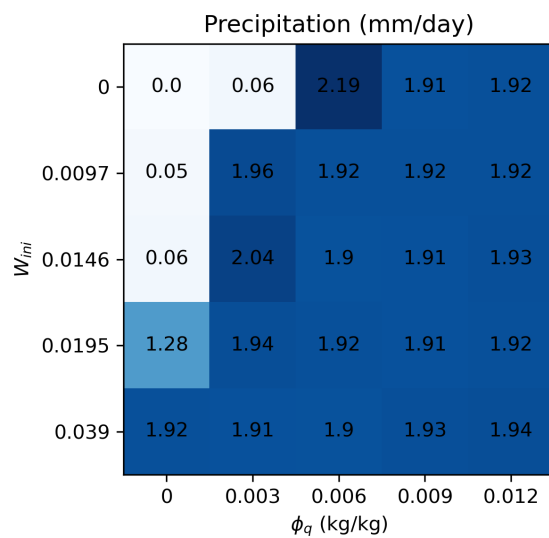


Figure C.2: Precipitation sensitivity in CM1 mode to initial subsurface water and initial atmospheric moisture.

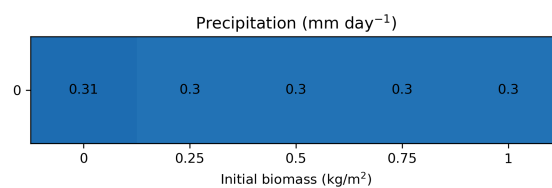


Figure C.3: Precipitation sensitivity in CM2 mode to initial biomass.

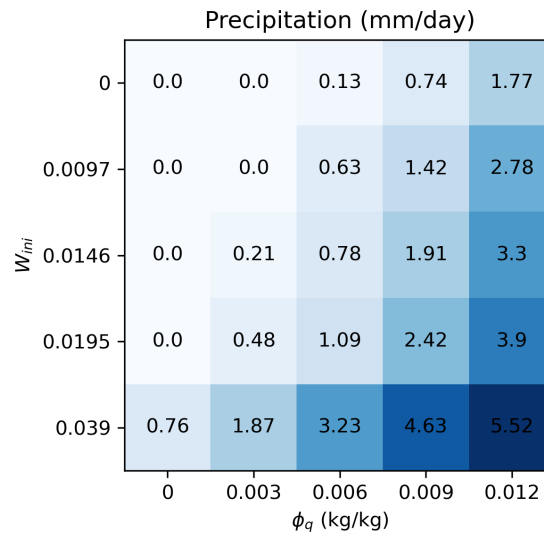


Figure C.4: Precipitation sensitivity in CM2 mode to initial subsurface water and initial atmospheric moisture.

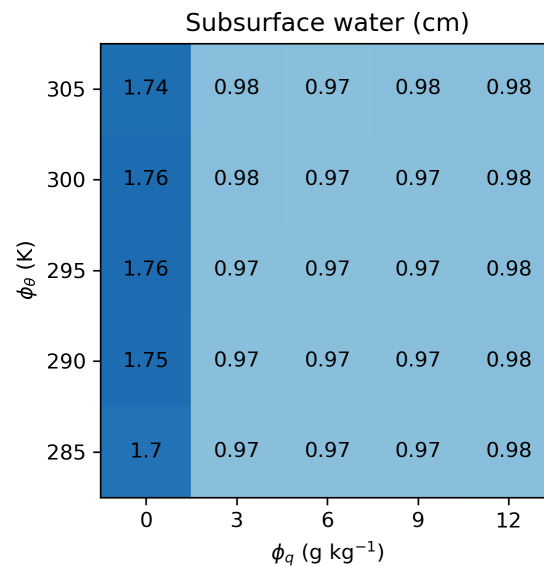
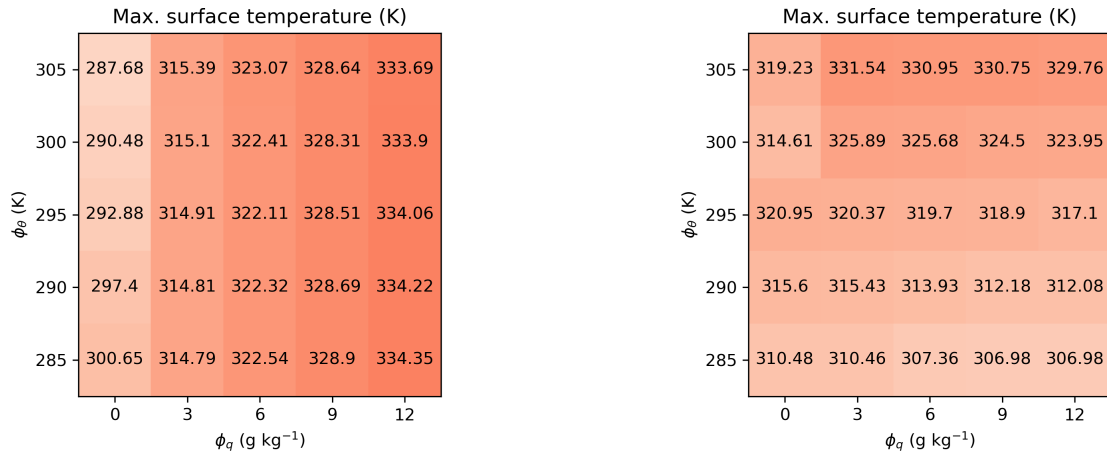


Figure C.5: Subsurface water sensitivity for an unconstrained atmospheric temperature (CM1 mode) but with a constant albedo of 0.3. The results shown here mostly match the corresponding results with a varying albedo (Figure 4.1a), except for the case where $\phi_q = 0$, where the equilibrium subsurface water goes towards 1.70-1.76 cm instead of showing a clear increase with ϕ_θ .



(a) Maximum surface temperature, unconstrained atmospheric temperature (CM1).

(b) Maximum surface temperature, constrained atmospheric temperature (CM2).

Figure C.6: Closed model sensitivity results for atmospheric moisture and atmospheric temperature parameters.

C.2 OM sensitivity

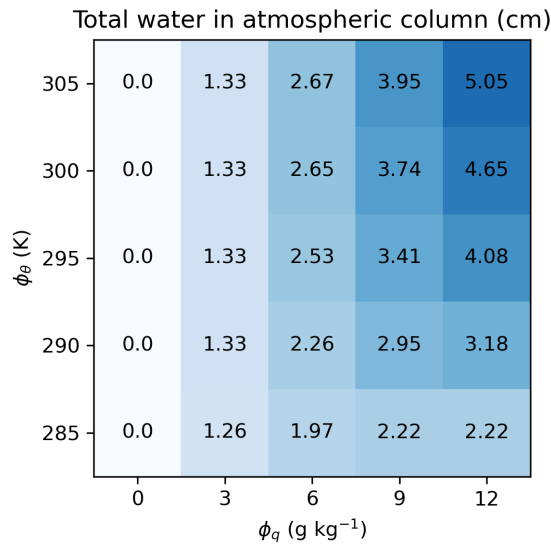


Figure C.7: The total amount of water in the atmospheric column (cm) in OM mode is almost fully determined by the boundary atmospheric moisture profile. However, for the moister profiles, the atmospheric temperature profile has an increased effect.

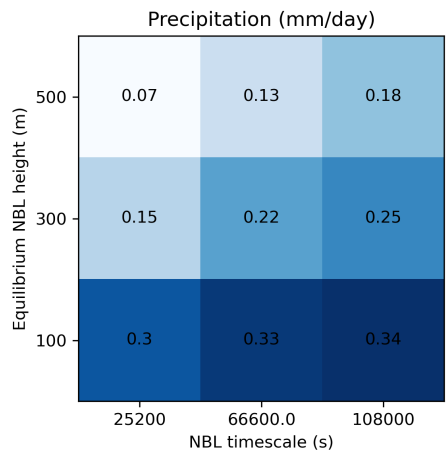


Figure C.8: Precipitation sensitivity in OM mode to NBL equilibrium height and timescale.

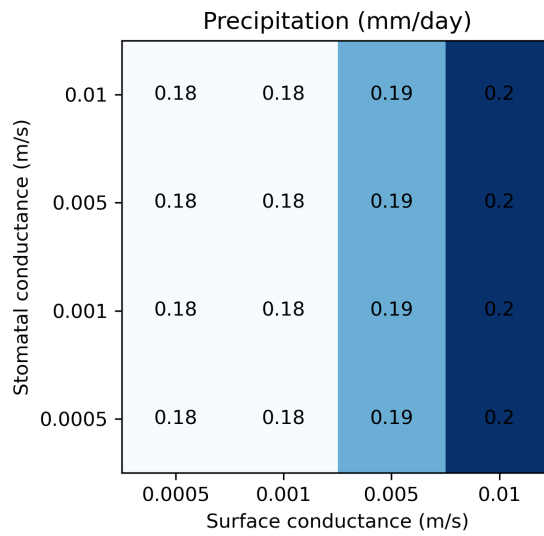


Figure C.9: Precipitation sensitivity in OM mode to surface and stomatal conductance.

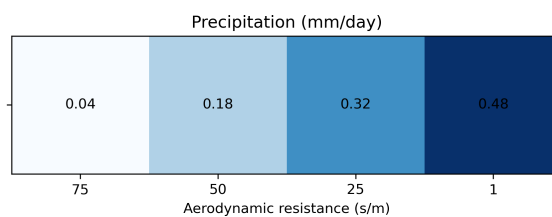


Figure C.10: Precipitation sensitivity in OM mode to aerodynamic resistance.

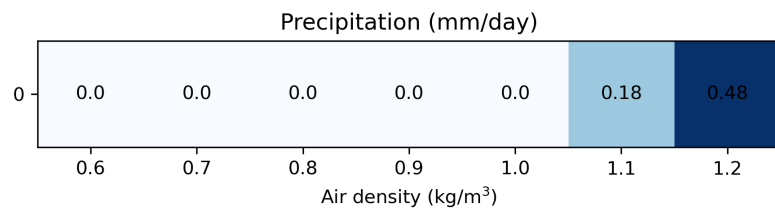


Figure C.11: Precipitation sensitivity in OM mode to the chosen constant air density.

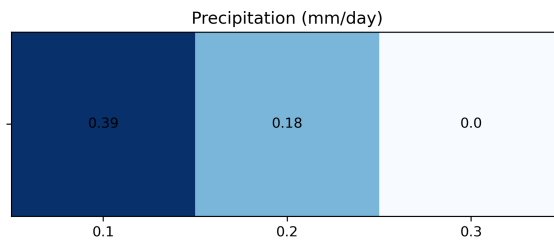


Figure C.12: Precipitation sensitivity in OM mode to the ratio of the sensible heat flux at the top of the ABL to the surface sensible heat flux.

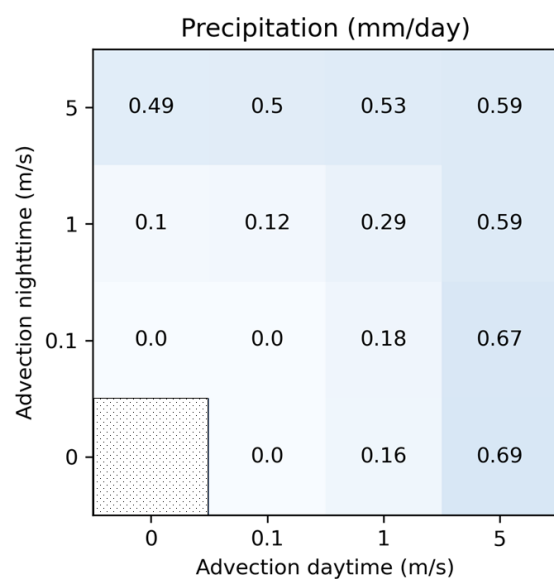


Figure C.13: Precipitation sensitivity in OM mode to wind speed during the day and during the night. The case without any wind is masked because this changes the mode of the model from open to closed.

C.3 OMT sensitivity

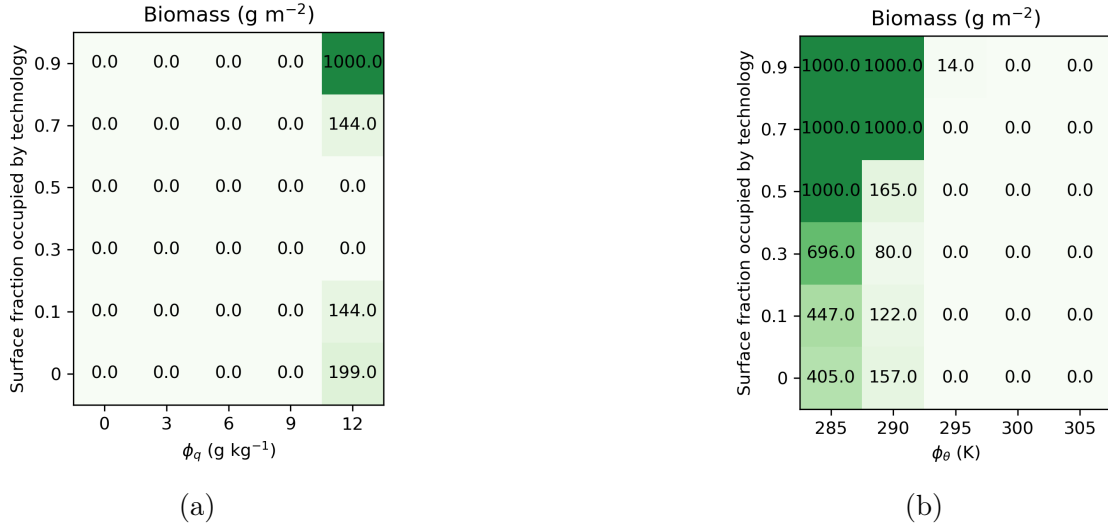


Figure C.14: Open model with technology (OMT mode) sensitivity vegetation biomass results for a varying surface fraction occupied by the technology. Surface fraction = 0 is equivalent to model runs in OM mode. For the panel on the left the boundary conditions for atmospheric specific humidity are varied and for the panel on the right the boundary conditions for the atmospheric temperature are varied. Results of the same runs for precipitation and subsurface water are shown in Figure 4.3.

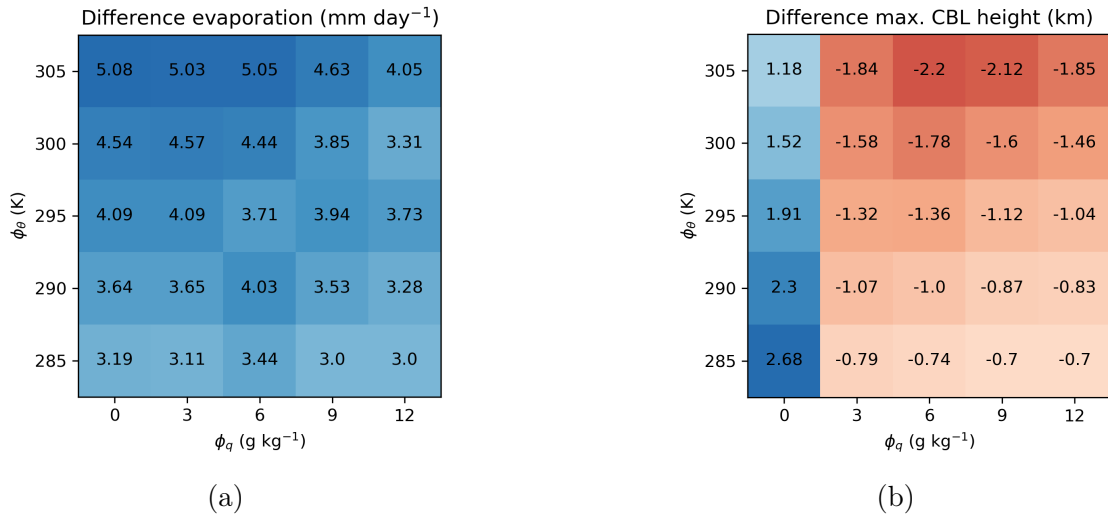


Figure C.15: OMTH mode differences compared to OM mode in (a) evaporation and (b) maximum convective boundary layer height.

C.4 Case studies

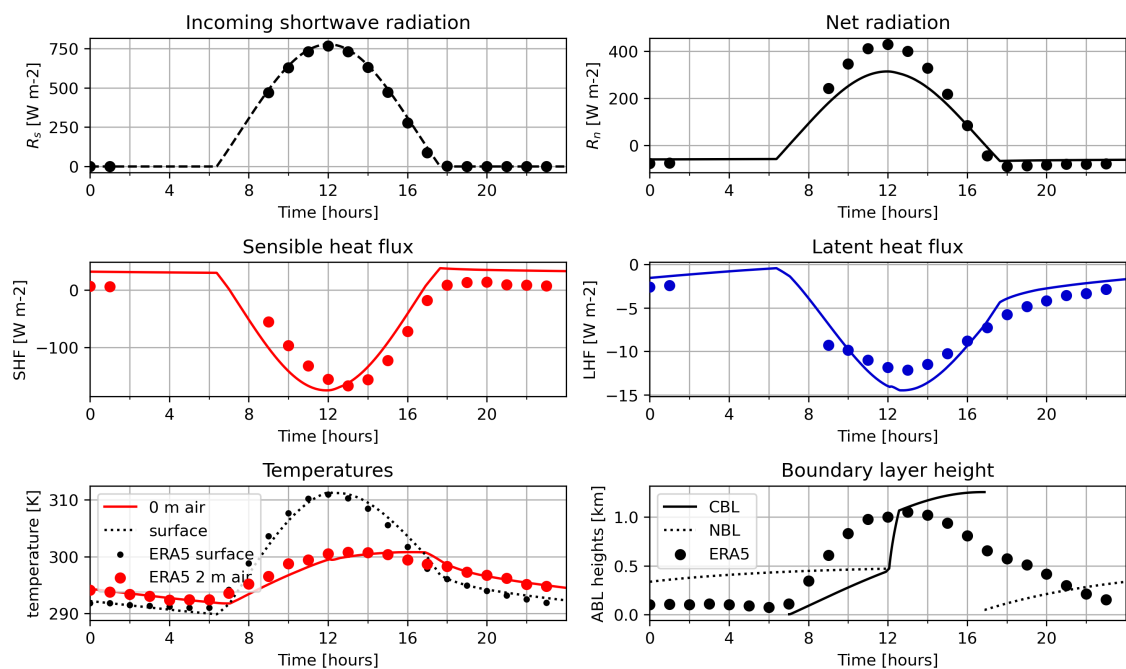


Figure C.16: Model fit for for the Sinai peninsula case study location 1. Dots represent ERA5 monthly averaged reanalysis by hour of day for the month of October in the year 2021. The radiative fluxes have missing values for hours 2-8. Lines are the model run where the model parameters are tuned to fit the ERA5 energy fluxes and temperatures. Boundary layer height is shown for comparison only, not for tuning.

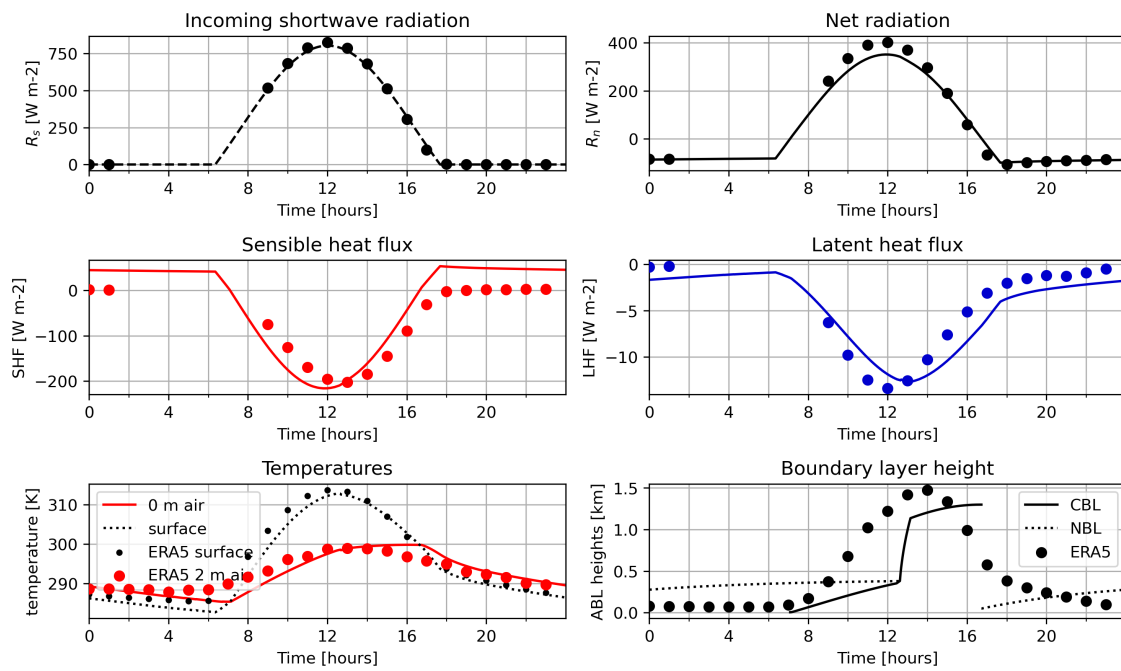


Figure C.17: Model fit for for the Sinai peninsula case study location 3. Dots represent ERA5 monthly averaged reanalysis by hour of day for the month of October in the year 2021. The radiative fluxes have missing values for hours 2-8. Lines are the model run where the model parameters are tuned to fit the ERA5 energy fluxes and temperatures. Boundary layer height is shown for comparison only, not for tuning.

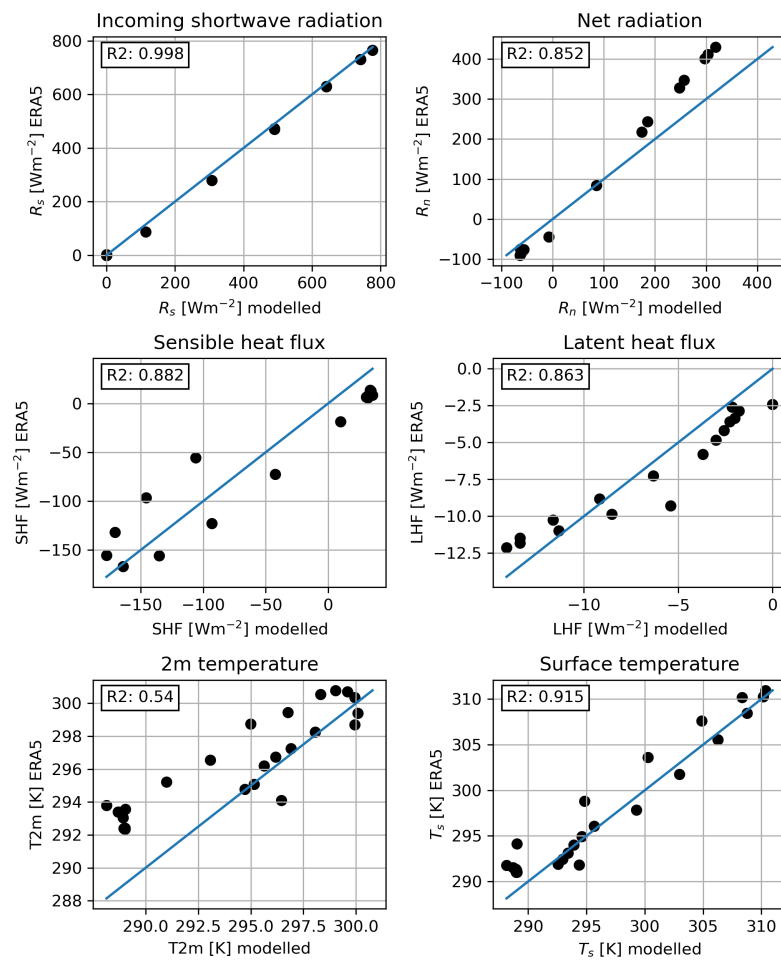


Figure C.18: Scatter plots of modelled variables on the x-axis and ERA5 reanalysis data on the y-axis for the Sinai peninsula case study location 1. Blue lines are 1:1 lines plotted as a reference. The coefficient of determination (R^2) is given.

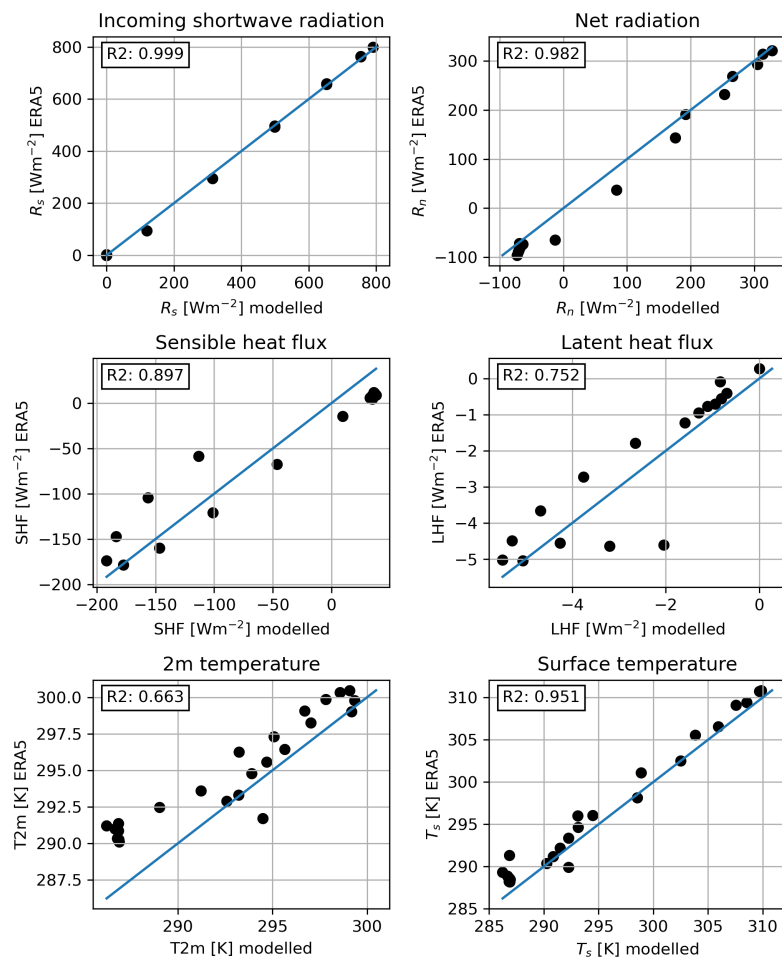


Figure C.19: Scatter plots of modelled variables on the x-axis and ERA5 reanalysis data on the y-axis for the Sinai peninsula case study location 2. Blue lines are 1:1 lines plotted as a reference. The coefficient of determination (R^2) is given.

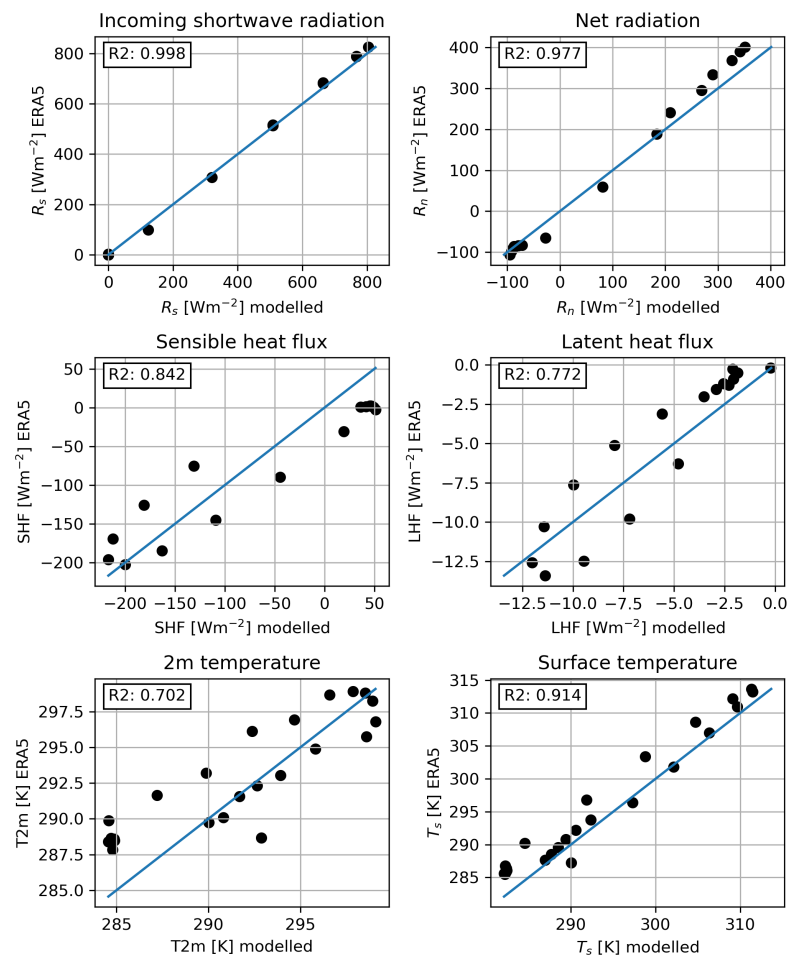


Figure C.20: Scatter plots of modelled variables on the x-axis and ERA5 reanalysis data on the y-axis for the Sinai peninsula case study location 3. Blue lines are 1:1 lines plotted as a reference. The coefficient of determination (R^2) is given.

Table C.1: Water fluxes and water and biomass states in equilibrium for the three Sinai case study locations, each for three different model runs. $\Delta x = 100$ km.

	Sinai 1			Sinai 2			Sinai 3		
	OM	OMTL	OMTH	OM	OMTL	OMTH	OM	OMTL	OMTH
Fluxes [mm/day]									
Advection in	5.80e+01	5.80e+01	5.80e+01	5.73e+01	5.73e+01	5.73e+01	4.23e+01	4.23e+01	4.23e+01
Advection out	5.81e+01	5.86e+01	6.00e+01	5.74e+01	5.81e+01	5.93e+01	4.27e+01	4.34e+01	4.47e+01
Precipitation	0.00e+00								
Orographic precipitation	5.81e-01	5.86e-01	5.97e-01	5.75e-01	5.81e-01	5.93e-01	4.27e-01	4.34e+01	4.47e-01
Evapotranspiration	5.52e-01	1.53e-01	1.16e-01	5.67e-02	1.90e-02	1.40e-02	8.63e-02	2.87e-02	2.04e-02
Evaporation technology	0.00e+00	6.91e-01	1.84e+00	0.00e+00	6.79e-01	1.84e+00	0.00e+00	7.78e-01	2.03e+00
Drainage	2.30e-01	4.34e-01	4.82e-01	5.19e-01	5.63e-01	5.79e-01	3.41e-01	4.06e-01	4.27e-01
States									
Atmosphere [mm]	2.04e+01	2.02e+01	1.99e+01	1.68e+01	1.67e+01	1.71e+01	1.03e+01	1.03e+01	1.17e+01
Surface [mm]	2.87e+00	5.43e+00	6.03e+00	6.48e+00	7.04e+00	7.24e+00	4.27e+00	5.08e+00	5.34e+00
Vegetation biomass [g/m ²]	3.41e-25	1.95e-22	1.16e-21	3.36e-23	1.72e-22	3.26e-22	4.07e-24	4.87e-23	1.08e-22

Table C.2: Water fluxes and water and biomass states in equilibrium for the three Sinai case study locations, each for three different model runs. $\Delta x = 1000$ km (reduced effect of advection).

	Sinai 1			Sinai 2			Sinai 3		
	OM	OMTL	OMTH	OM	OMTL	OMTH	OM	OMTL	OMTH
Fluxes [mm/day]									
Advection in	5.80e+00	5.80e+00	5.80e+00	5.73e+00	5.73e+00	5.73e+00	4.23e+00	4.23e+00	4.23e+00
Advection out	5.83e+00	6.67e+00	7.57e+00	5.76e+00	6.60e+00	7.50e+00	4.28e+00	5.22e+00	6.28e+00
Precipitation	0.00e+00	0.00e+00	4.04e-02	0.00e+00	0.00e+00	2.67e-03	0.00e+00	0.00e+00	2.02e+00
Orographic precipitation	5.83e-02	6.67e-02	7.57e-02	5.76e-02	6.60e-02	7.50e-02	4.29e-02	5.22e-02	6.28e-02
Evapotranspiration	4.75e-02	3.57e-02	3.96e-02	1.60e-02	6.28e-03	4.02e-03	1.72e-02	8.21e-03	5.95e-03
Evaporation technology	0.00e+00	8.72e-01	1.79e+00	0.00e+00	8.49e-01	1.75e+00	0.00e+00	9.55e-01	2.02e+00
Drainage	1.08e-02	3.12e-02	7.26e-02	4.67e-02	6.00e-02	7.40e-02	2.57e-02	4.44e-02	5.74e-02
States									
Atmosphere [mm]	2.08e+01	2.42e+01	2.51e+01	1.76e+01	2.05e+01	2.19e+01	1.03e+01	1.31e+01	2.05e+01
Surface [mm]	1.34e-01	3.90e-01	9.07e-01	5.21e-01	7.50e-01	9.25e-01	3.21e-01	5.55e-01	7.18e-01
Vegetation biomass [g/m ²]	9.50e-27	2.42e-26	3.67e-26	6.66e-28	7.61e-28	8.11e-28	2.99e-26	4.19e-26	4.64e-26

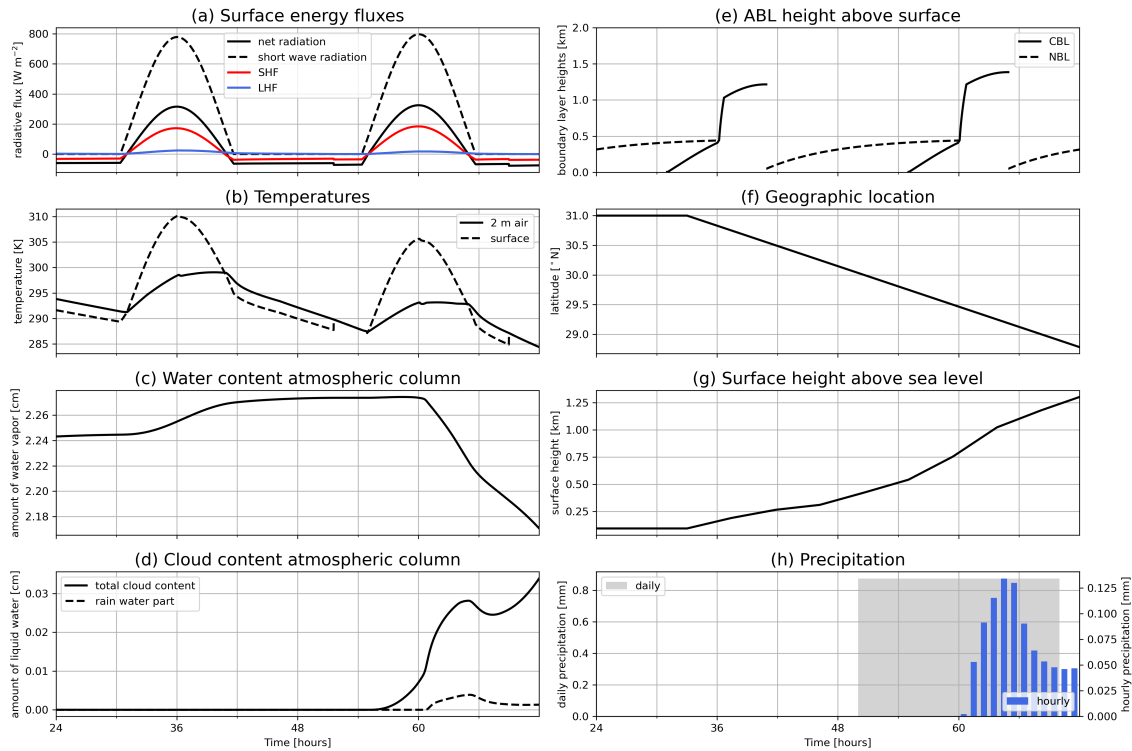


Figure C.21: Time series of the run in moving column mode (MCM) where the first 33 hours are stationary after which the air column moves southward with a speed of 1.75 m s^{-1} . The first 24 hours of the run are not shown. Panel a: Surface energy fluxes [W m^{-2}] with the incoming shortwave solar radiation (black, dashed), the net radiation (black, solid), the sensible heat flux (red), and the latent heat flux (blue). Panel b: Temperatures [K] of the surface (dashed) and near the surface (solid). Panel c: Water content [cm] of the atmospheric column up to 5 km high. Panel d: As panel c but for the cloud content (solid) and the rain water part of the cloud content (dashed). Panel e: Atmospheric boundary layer height [km] of the convective boundary layer (solid) and the nocturnal boundary layer (dashed). Panel f: Latitude of the geographic location [$^{\circ}\text{N}$]. Panel g: Height of the surface above sea level [km]. Panel h: Daily (grey) and hourly (blue) precipitation [mm].

C.5 Discussion

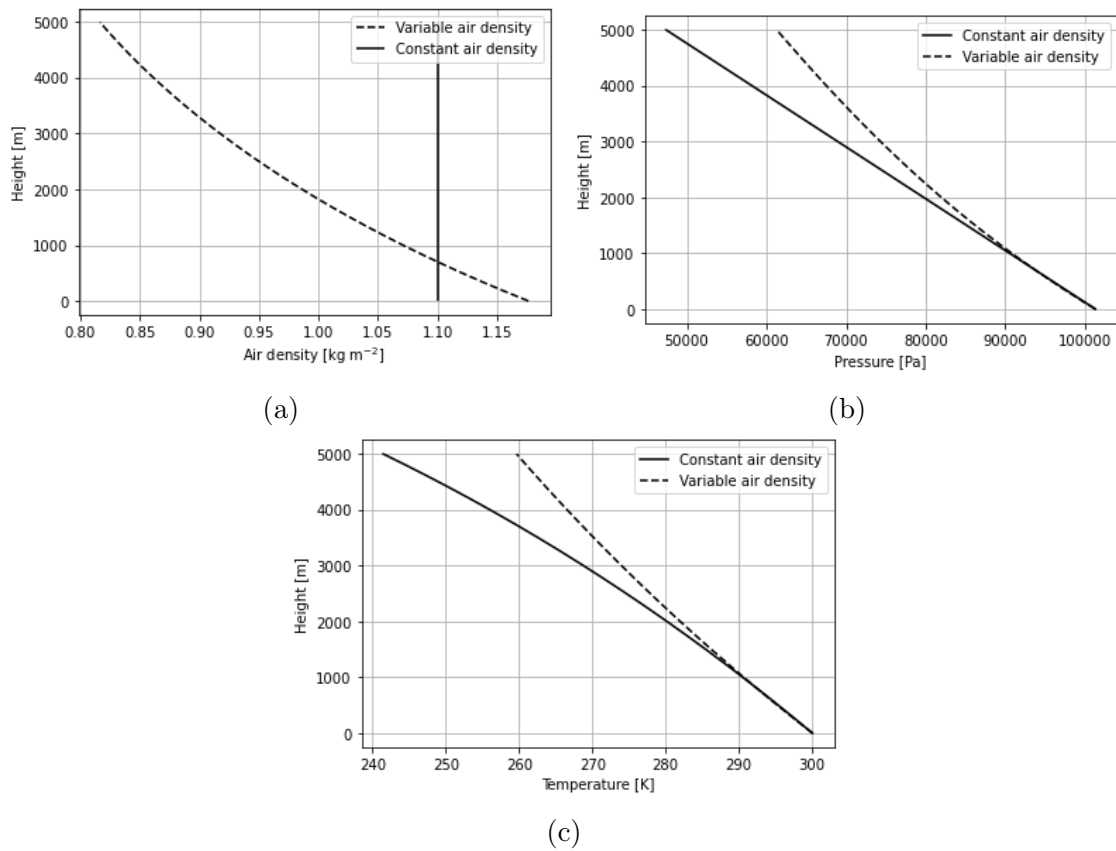


Figure C.22: Example of the increasing differences in air density (a), pressure (b) and temperature (c) with height between atmospheres where the air density is assumed constant as used in this research (solid lines) and the more realistic case where the air density decreases with height (dashed lines). The potential temperature of this example is constant with height.